



High-efficiency degradation of carbamazepine by the synergistic electro-activation and bimetal (FeCo@NC) catalytic-activation of peroxymonosulfate

Shuaishuai Li^a, Minghua Zhou^{a,*}, Huizhong Wu^a, Ge Song^a, Jiana Jing^a, Nuo Meng^a, Wei Wang^{a,b,**}

^a MOE Key Laboratory of Pollution Processes and Environmental Criteria, Tianjin Key Laboratory of Environmental Technology for Complex Trans-Media Pollution, Tianjin Advanced Water Treatment Technology International Joint Research Center, College of Environmental Science and Engineering, Nankai University, Tianjin 300350, China

^b Nankai Cangzhou Bohai New Area Green Chemical Research Co., Ltd, Cangzhou 061108, China

ARTICLE INFO

Keywords:

FeCo alloy nanocatalyst
Electrochemical activation
Peroxymonosulfate
Radical and nonradical mechanisms
Carbamazepine

ABSTRACT

This study developed a novel advanced oxidation process, coupling activation of peroxymonosulfate (PMS) by electrochemistry and catalyst based on an advanced electrocatalyst. Herein, nitrogen-rich porous carbon decorated with FeCo alloy (FeCo@NC) was fabricated to modify carbon felt (FeCo@NC/CF) to remove carbamazepine (CBZ) via electro-enhanced activation of PMS (E-FeCo@NC/CF-PMS). C–C, O–C=O and M=O contents in FeCo@NC are positively correlated with CBZ degradation ($r^2 = 0.937$ and 0.942). Benefit from the obvious synergistic effect ($S=3.49$) of electro-activation and catalytic-activation caused by electrowetting, CBZ removal ($k = 0.0811 \text{ min}^{-1}$) was significantly improved with extremely low electric energy consumption (EEC, $0.0506 \text{ kWh log}^{-1} \text{ m}^{-3}$). Electric field facilitates the regeneration of key catalytic components Fe^{2+} and Co^{2+} . $\cdot\text{OH}$ (derived from the co-activation) and electron-transfer process (derived from catalytic-activation) were the underlying catalysis mechanisms. This work provided new vision to promote the practical utilization of Fenton-like reaction with high-efficiency and low-cost.

1. Introduction

Advanced oxidation processes (AOPs) have been considered as an operative environmental remediation technology for the removal of organic contaminants from the water environment. Among various AOPs, Fenton-like reactions based on PMS have attracted extensive research interests due to their advantages of wider pH adaptation range and easier activation to produce a variety of reactive oxygen species (ROS, such as hydroxyl radicals ($\cdot\text{OH}$), sulfate radicals ($\text{SO}_4^{\cdot-}$), superoxide anion ($\text{O}_2^{\cdot-}$) and singlet oxygen ($^1\text{O}_2$)) [1].

Previous studies have shown that carbon-based materials such as carbon nanotubes, graphene and nano-diamond exhibit good activity in activating PMS to degrade pollutants [2], and the introduction of heteroatoms (N, P, S etc.) into the carbon skeleton can improve the

charge/spin redistribution of the carbon skeleton and form more catalytic centers [2]. However, the poor stability of carbonaceous catalysts greatly limits their reusability as the loss of active center during the catalytic reaction [3]. Interestingly, enhanced interactions between carbon and metal species have been observed when doping carbon with heteroatom N. The variations of electronegativity among carbon and N atoms rearranges the charge distribution and structural defects of carbon to promote the interaction between metal and heteroatoms and avoid agglomeration [4]. The metal- $\text{N}_x\text{-C}$ (metal = Mn, Fe, Co, Ni, Cu) coordination structure is often the key reaction center of PMS activation or organic degradation [3,5,6].

In view of this, metal nanoparticles (NPs) modified N-doped porous carbon (M/NC) are considered as one of the most potential candidates due to the synergies between carbon skeleton and metal center [3,7]. Yu

* Corresponding author.

** Corresponding author at: MOE Key Laboratory of Pollution Processes and Environmental Criteria, Tianjin Key Laboratory of Environmental Technology for Complex Trans-Media Pollution, Tianjin Advanced Water Treatment Technology International Joint Research Center, College of Environmental Science and Engineering, Nankai University, Tianjin 300350, China.

E-mail addresses: zhoumh@nankai.edu.cn (M. Zhou), nkwangwei@126.com (W. Wang).

<https://doi.org/10.1016/j.apcatb.2023.123064>

Received 15 March 2023; Received in revised form 28 June 2023; Accepted 30 June 2023

Available online 3 July 2023

0926-3373/© 2023 Elsevier B.V. All rights reserved.

et al. demonstrated that loading cobalt nanoparticles into graphene shells could produce strong interfacial interactions, thus providing optimal active sites with low adsorption energy for PMS accumulation, which enabled the generation of highly oxidizing NG-PMS* intermediates [8]. Zhao et al. reported the synthesis of Fe₃C/Fe decorated N-doped magnetic carbon materials, which showed a good activation of PMS due to the coexistence of C- π group, N-doped species and iron nanoparticles [7]. Although great progress has been made in the activation of PMS by M/NC, the performance of catalysts is generally limited by the discontinuous band structure of a single metal, which makes it difficult to accurately adjust the electronic structure to the optimal state [9,10]. In contrast, due to the introduction of complementary metal elements, bimetallic alloys can help adjust the electronic structure and provide more reaction centers for PMS activation, thus significantly improving catalytic activity. For example, Zhao et al. showed that an unprecedented double active sites was constructed on the FeCo-N/Cx, in which FeCo alloy could reduce the energy barrier of O-O bond breaking in PMS molecule, thus forming high valence FeCo=O active substance and singlet oxygen. In addition, the introduction of Fe into Co-N/C to form a diatomic FeCo-N coordination structure can prevent the leaching of Co ions [11]. Although some excellent work has been reported, rapid and simple synthesis of nano-particles functionalized NC catalysts for bimetallic alloy remains challenging. And further studies are needed to explore the active sites and the reaction mechanisms related to organic degradation.

It is important to note that for the radical associated PMS activation pathway caused by electron transfer, low-valence metal is required to transfer electrons to PMS molecule to cleave the O-O of the PMS, resulting in the production of $\cdot\text{OH}$ or $\text{SO}_4^{\cdot-}$ [12]. Therefore, the limited reduction and regeneration of high-valence metals to low-valence metals is the key factor limiting the reusable performance of catalysts [13]. In addition, although the heterogeneous catalytic system overcomes the defects of homogeneous metal ion recovery and narrow pH range [14], its complex recovery process or expensive reactor design requiring gross agent input is a key bottleneck restricting the practical use of almost all highly reactive nanocatalysts [15].

Fortunately, electrochemical advanced oxidation processes (EAOPs) are promising to provide a practical solution to these bottlenecks [16]. For example, Long et al. used an electrochemical system as "co-catalyst" where cathodic reduction reactions promoted electron transfer to Fe(III) and triggered a sustainable Fe(III)/Fe(II) redox cycle to enhance the activation of PMS (EC/Fe (III)/PMS) [17]. Jin et al. used Fe single-atom functionalized MXene as the cathode to effectively solve the problem of low PMS activation efficiency caused by complex recovery process of heterogeneous catalysts and poor mass transport in traditional batch reactors [18]. Notably, it has been shown that the distinct advantage of EAOPs is that it can accelerate the electron transfer between electron donor and acceptor, and the electric field significantly promotes the electrochemical activation of persulfate, resulting in the production of more radicals [19]. However, the activation of PMS by the original carbonaceous cathode often results in a lower reaction rate and higher energy consumption, and the stability of long-term operation is not ideal. Fortunately, coupling the highly active nano-catalyst with the carbonaceous cathode can complement each other's advantages and make up for their weaknesses [20]. However, the activation path of PMS and the degradation mechanism of organic molecules at the coupling cathode interface under the effect of electric field still need to be further studied.

For the above reasons, a nitrogen-rich porous carbon catalyst decorated with FeCo alloy nanoparticles (FeCo@NC) was designed and synthesized by a simple and scalable one-step pyrolysis method based on the strategy of changing the electronic structure to improve the catalytic efficiency in this study. Different from previous studies, CF and FeCo@NC catalysts were combined to prepare composite electrodes (FeCo@NC/CF). This method is universal and can be combined with others nano-catalysts, so as to overcome the bottleneck of low efficiency

and short life of CF electrode, difficult recovery of nano-catalyst and regeneration of effective active site in the electroactivated PMS system [21]. Carbamazepine (CBZ) was chosen as the target trace organic compounds (TrOCs) due to its prevalence in drinking water, municipal wastewater and wastewater sludge and resistance to common oxidants (e.g., chlorine, chlorine dioxide, hydrogen peroxide and PMS/PDS) [22]. The average concentration of CBZ in water bodies is $0.187 \mu\text{g L}^{-1}$ and the maximum even reaches $8.05 \mu\text{g L}^{-1}$ [23]. Carbon felt was chosen as the catalyst substrate due to its high surface area and porosity, which can provide abundant redox reaction sites, excellent electrolytic efficiency and mechanical stability at relatively low cost [9]. The coupling activation of PMS by electro-activation and FeCo@NC catalysis exhibited excellent synergistic effect, significantly accelerated the degradation of CBZ and reduced energy consumption. Importantly, it was found that electrowetting is responsible for the high synergistic effect. And the electric field promoted the effective regeneration of low-valence metal species, thus maintaining high activity of FeCo@NC/CF during recycling. In addition, dynamic analysis, radical quenching, EPR analysis and electrochemical test were used to reveal the active species and relative contributions. Moreover, we evaluated the environmental applicability to actual water bodies and the reuse performance of E-FeCo@NC/CF-PMS process. Our study can provide a reference for the coupling activation of PMS by electro-activation with multiple high-efficiency catalysts, and promote the practical utilization of PMS based AOPs for reducing energy consumption and post-treatment cost.

2. Experimental sections

2.1. Preparation of catalyst and cathode

FeCo@NC was synthesized by a simple and scalable thermal decomposition method (Fig. S1). Typically, melamine (2.0 g), α -cyclodextrin (α -CyD) (0.4 g), Fe(NO₃)₃•9 H₂O (0.02025 g) and Co(NO₃)₂•6 H₂O (0.1355 g) were dispersed into a mixed solution contained 80 mL distilled water and 20 mL methanol with vigorous stirring for 15 min. Then, the mixture was transferred to an oil bath at 80 °C. The sediment was finely ground after the solution was completely dried. Then the as-prepared powder was pyrolyzed in N₂ atmosphere at 550 °C for 3 h firstly and further annealed at 900 °C for 6 h with a heating rate of 5 °C min⁻¹. The obtained products were marked as FeCo@NC. Similarly, NC, Fe@NC and Co@NC were synthesized without adding Fe(NO₃)₃•9 H₂O and Co(NO₃)₂•6 H₂O, adding only Fe(NO₃)₃•9 H₂O or Co(NO₃)₂•6 H₂O, respectively. In addition, based on the total molar number of 1 mmol, FeCo@NC (2:1) and FeCo@NC (1:2) were prepared with the molar ratio of Fe/Co at 2:1 and 1:2, respectively. The FeCo@NC-0.25 or FeCo@NC-0.75 were synthesized by adjusting the amount of Fe(NO₃)₃•9 H₂O and Co(NO₃)₂•6 H₂O to 0.25 or 0.75 mmol in the molar ratio of Fe/Co at 1:1.

The cathode was prepared as follows:

CF cathode: commercial carbon felt (electrode size: 2 *5 cm, actual water contact area: 2 *3 cm, the rest of electrode plate is used to connect electrode clips) was soaked in acetone and deionized water and ultrasonic treated for 2 h, and then dried in an oven at 80 °C.

FeCo@NC/CF cathode: CF (2 × 5 cm) was used as the FeCo@NC carrier, where the 2 × 3 cm area was used to coat the catalyst ink and the rest area was used to attach the electrode clips. Specifically, 15 mg FeCo@NC catalysts were distributed evenly through ultrasound into 1 mL ethanol containing 50 μL Nafion (5 wt%). The obtained ink was evenly coated on the CF working area with a catalyst loading of 2.5 mg cm^{-2} . The prepared cathode was denoted as FeCo@NC/CF and used in the electrochemical water treatment after naturally dried in the air. Similarly, to explore the CBZ removal performance of different catalysts, the corresponding catalysts were used to coat CF to prepare modified cathodes.

2.2. Experimental procedures

2.2.1. Degradation experiment

The as-prepared FeCo@NC/CF cathode (2 cm × 3 cm), and a dimensionally stable anode (Ti/RuO₂-IrO₂, DSA, 2 cm × 3 cm) were used to conduct degradation experiment (electrode spacing was 1.5 cm) in a 150 mL beaker containing Na₂SO₄ (50 mM) and 100 mL contaminant solution with a magnetic stirrer at room temperature. 0.1 M H₂SO₄ and 0.1 M NaOH were used to adjust solution pH. During the degradation experiment, 0.25 mL solution was extracted at given intervals and mixed with 1 mL methanol and 1.25 mL ultrapure water to quench the excess radicals and dilute the electrolyte concentration. The mixed solution was filtered through a 0.22 μm film. The concentration of target pollutants was determined by high-performance liquid chromatograph (HPLC, Ultimate 3000, ThermoFisher, America) equipped with C18 column (3 μm, φ3.0 × 100 mm), and the detection methods of different pollutants (eg. sulfamethazine (SMT), atrazine (ATZ), 2,4-dichlorophenol (2,4-DCP), tetracycline (TC)) were listed in Table S1. For the quenching experiment, a series of quenching agents, such as tert-butanol (TBA, 10 mM), MeOH (500 mM), furfuryl alcohol (FFA, 5 mM) were separately added to the solution to explore possible ROS. The intermediates of CBZ degradation were detected by liquid chromatography coupled with a mass spectrometer (LC-MS/MS, 6460 Triple Quad, Agilent, USA) using a Waters ACQUITY UPLC BEH C18 analytical column (1.7 μm, 2.1 × 50 mm) in positive ESI mode.

2.2.2. Electrochemical analysis

Electrochemical impedance spectroscopy (EIS) and Tafel plot of each catalysts were performed using CHI 760E potentiostat (CH Instruments, Chenhua, Shanghai, China) in 50 mM Na₂SO₄ solution with a three-electrode cell. To prepare the working electrode, 5 mg catalyst was added into 1 mL ethanol containing 50 μL 5 wt% Nafion, followed by ultrasonication for 30 min to make full dispersion of ink, and then 10 μL ink was dropped on a glassy carbon electrode. The catalyst loading amount was 0.25 mg cm⁻². The counter electrode and reference electrode was platinum electrode and Ag/AgCl electrode (saturated KCl) respectively, and the potentials were converted to the reversible hydrogen electrode (RHE) reference scale using the Nernst equation: E (vs. RHE) = E (vs. Ag/AgCl) + 0.224 V + 0.0591 × pH [24].

The cyclic voltammetry (CV) was measured at a scanning rate of 100 mV s⁻¹ in 1 M KCl containing 10 mM K₃[Fe(CN)₆] to analyzing the electroactive surface area (EASA) with Randles-Sevcik Eq. (1) [24]:

$$I_p = 2.69 \times 10^5 \times n^{3/2} \times A \times D^{1/2} \times C \times v^{1/2} \quad (1)$$

where I_p is the peak current (A), n is the number of electrons contributing to the redox reaction, D is the diffusion coefficient (6.3×10^{-6} cm² s⁻¹), C is the concentration of Fe(CN)₆⁴⁻ in the bulk solution (mol cm⁻³), v is the scan rate (V s⁻¹), and A is the EASA (cm²).

Chronopotentiometry and chronoamperometry analyses were carried to obtain the surface oxidation potential response of the catalyst, PMS and CBZ samples were added into the electrolyte at stated intervals with final concentrations of 1.5 mM and 10 mg L⁻¹, respectively. Chronoamperometry analyses were carried out at various cathode potentials to monitor the current values after the addition of PMS and CBZ samples.

2.3. Analytical methods

The apparent first-order rate constant for the oxidation of CBZ was determined according to the Eq. (2), suggesting that it follows a pseudo first order reaction kinetics model [25].

$$\ln \left(\frac{C_0}{C_t} \right) = kt \quad (2)$$

where C_0 is the initial concentration of pollutant (mg L⁻¹), C_t is the

concentration of pollutant at t min (mg L⁻¹), and t is the reaction time (min), k is the rate constant (min⁻¹).

The synergistic factor (S) was calculated using Eq. (3) to quantify the interaction degree among multiple processes [26,27].

$$S_{a-b} = \frac{k_{obs,ab}}{k_{obs,a} + k_{obs,b}} \quad (3)$$

where S_{a-b} is the synergistic factor of multiple processes “a” or “b” involved in the coupling system, $k_{obs,ab}$, $k_{obs,a}$, $k_{obs,b}$ are the apparent kinetic constants in the coupling system or independence process.

The electrical energy per order (EEC (kWh log⁻¹ m³)) for pollutants removal was calculated as follows: [28,29].

$$EEC = \frac{UIT}{V \log \frac{C_0}{C_t}} \quad (4)$$

where U , I , T and V represent the voltage (V), current (A), reaction time (h), volume (L), respectively; C_0 and C_t represent initial and final concentrations of pollutants (mg L⁻¹), respectively.

The steady concentrations of $\bullet OH$ ($[\bullet OH]_{ss}$), $SO_4^{\bullet -}$ ($[SO_4^{\bullet -}]_{ss}$) or 1O_2 ($[^1O_2]_{ss}$) during the degradation of CBZ by E-FeCo@NC/CF-PMS process were explored by use 0.05 mM nitrobenzene (NB) or benzoic acid (BA) and furfuryl alcohol (FFA) as probe, respectively [30,31]. NB has a higher second-order rate constant of $k_{NB, \bullet OH}^{\bullet} = 3.9 \times 10^9$ M⁻¹ s⁻¹ with $\bullet OH$ compared with $SO_4^{\bullet -}$ ($k_{NB, SO_4^{\bullet -}} \leq 10^6$ M⁻¹ s⁻¹) [30,32], whereas BA has a high reaction rate constant both for $\bullet OH$ ($k_{BA, \bullet OH} = 2.1 \times 10^9$ M⁻¹ s⁻¹) and $SO_4^{\bullet -}$ ($k_{BA, SO_4^{\bullet -}} = 1.2 \times 10^9$ M⁻¹ s⁻¹). It should be noted that, in addition to having a higher rate constant with 1O_2 ($k_{FFA, ^1O_2} = 1.2 \times 10^8$ M⁻¹ s⁻¹), FFA also has a higher rate constant with both $\bullet OH$ and $SO_4^{\bullet -}$. As shown in Table S2, the $[\bullet OH]_{ss}$, $[SO_4^{\bullet -}]_{ss}$ and $[^1O_2]_{ss}$ could be obtained as follows [30,31]. The mathematical deduction of the Eqs. (5–11) is in Text S3.

$$[\bullet OH]_{ss} = \frac{k_{obs,NB}}{k_{NB, \bullet OH}} \quad (5)$$

$$[SO_4^{\bullet -}]_{ss} = \frac{k_{obs,BA} - k_{BA, \bullet OH} [\bullet OH]_{ss}}{k_{BA, SO_4^{\bullet -}}} \quad (6)$$

$$[^1O_2]_{ss} = \frac{k_{obs,FFA} - k_{FFA, \bullet OH} [\bullet OH]_{ss} - k_{FFA, SO_4^{\bullet -}} [SO_4^{\bullet -}]_{ss}}{k_{FFA, ^1O_2}} \quad (7)$$

where, [NB], [BA] and [FFA] represent the concentrations of NB, BA and FFA at a given reaction time, respectively; [NB]₀, [BA]₀ and [FFA]₀ are the initial concentrations of NBA, BA and FFA, respectively.

The contributions of $SO_4^{\bullet -}$, $\bullet OH$, 1O_2 and ETP to CBZ degradation were calculated as follows [30,31]:

$$R_{\bullet OH} = \frac{k_{CBZ, \bullet OH} [\bullet OH]_{ss}}{k_{obs,CBZ}} \quad (8)$$

$$R_{SO_4^{\bullet -}} = \frac{k_{CBZ, SO_4^{\bullet -}} [SO_4^{\bullet -}]_{ss}}{k_{obs,CBZ}} \quad (9)$$

$$R_{^1O_2} = \frac{k_{CBZ, ^1O_2} [^1O_2]_{ss}}{k_{obs,CBZ}} \quad (10)$$

$$R_{else} = 1 - R_{\bullet OH} - R_{SO_4^{\bullet -}} - R_{^1O_2} \quad (11)$$

where, $k_{CBZ, \bullet OH}$, $k_{CBZ, SO_4^{\bullet -}}$ and $k_{CBZ, ^1O_2}$ are the second-order rate constant of CBZ with $\bullet OH$ (8.8×10^9 M⁻¹ s⁻¹), $SO_4^{\bullet -}$ (1.92×10^9 M⁻¹ s⁻¹) and 1O_2 (2.57×10^5 M⁻¹ s⁻¹), respectively; $k_{obs,CBZ}$ is the pseudo-first-order rate constant of CBZ; $R_{\bullet OH}$, $R_{SO_4^{\bullet -}}$, $R_{^1O_2}$ and R_{else} , are the relative contribution of $SO_4^{\bullet -}$, $\bullet OH$, 1O_2 and ETP, respectively.

2.4. DFT calculations

The Vienna ab initio simulation program (VASP5.4.1) uses the Perdew-Burke-Ernzerhof (PBE) approach to implement first-principles calculations [25]. A planar wave cut-off energy of 400 eV was used within the framework of the projective augmented wave method. Using the k-point set created by Monkhorst-Pack to integrate the Brillion area, it was discovered that a $3 \times 3 \times 1$ k-point grid was adequate for calculating convergence. All atoms were converged to 0.01 eV/Å.

3. Results and discussion

3.1. Characterization of as-prepared catalysts

It is well known that graphite carbon nitride is prone to decompose at high temperatures. To increase the yield of NC, we introduced α -CyD as a stabilizer, which has a hexagonal cavity configuration with hydroxyl exposed boundary. This can generate hydrogen bond networks with MC and regulate the structure of the generated supramolecular precursors [33]. The morphology and microstructure of the prepared catalyst were observed by HRTEM. It can be seen that NC exhibits a thin layer graphitized carbon structure, and the lattice spacing of 0.34 nm is related to the (002) crystal plane of graphitized carbon (Fig. 1a-b). Interestingly, it can be clearly observed in the HRTEM micrographs of FeCo@NC (Fig. 1c) that a lot of dark contrasting nanoparticles with an average size of 25–60 nm are uniformly distributed and wrapped under a well-defined carbonaceous shell. The crystalline lattice fringe spacing of 0.21 nm presented in Fig. 1d was corresponded to the (211) crystal plane of FeCo alloy. In addition, a distinct graphite shell layer structure was found with a lattice spacing was 0.34 nm, corresponding to the (002) plane of graphite carbon. This graphite-carbon encased metal core-shell structure will strongly protect the metal from corrosion and

increase the stability of the active site, which can also be demonstrated in subsequent catalyst characterization analysis after the reaction [34, 35]. Furthermore, the EDX images verified the uniform permutation of C, N, Fe and Co elements, and the overlapping distribution of Fe and Co elements further confirmed the generation of FeCo alloy NPs (Fig. 1e-i) [36]. In addition, the TEM images of Fe@NC and Co@NC (Fig. S2) proven that they have similar morphology.

The XRD spectra of NC, Fe@NC, Co@NC and FeCo@NC were shown in Fig. 2a. Almost all the samples show a wide diffraction peak corresponding to the graphitic carbon (002) crystal plane at about 26.1° , which became stronger and sharper after the introduction of metal, indicating that metal could improve the degree of graphitization [7]. The characteristic diffraction peaks of Fe^0 (JCPDSNO.06–0696) or Co^0 (JCPDSNO.15–0806) appeared after the addition of iron or cobalt. Whereas three distinct diffraction peaks corresponding to the (110) (200) and (211) crystal plane of FeCo alloy (JCPDSNO.44–1433) at around 44.8° , 65.2° and 82.6° appeared after the introduction of bimetal, and no other evident peaks were found, indicating FeCo alloy has been successfully formed in the carbon layer.

Raman spectra were used to further analyze the structural characteristics and graphitization degree of the samples (Fig. 2b). The I_D/I_G values of NC, Co@NC, Fe@NC and FeCo@NC were 0.95, 0.84, 0.74 and 0.69, respectively, which demonstrated the high graphitization of all carbonaceous samples [7]. Notably, compared with NC, the I_D/I_G values decreased significantly after the introduction of metal elements. In addition, the I_D/I_G value of FeCo@NC dropped to 0.69, was significantly lower than that of Co@NC and Fe@NC, indicating that the synergistic effect between Fe and Co makes FeCo@NC has the strongest sp^2 hybrid structure [37].

The N_2 adsorption-desorption isotherms of NC, Co@NC, Fe@NC, and FeCo@NC (Fig. 2c) all showed typical types IV curve and H_4 -type hysteresis loop, reflecting the presence of mesoporous structures. It was

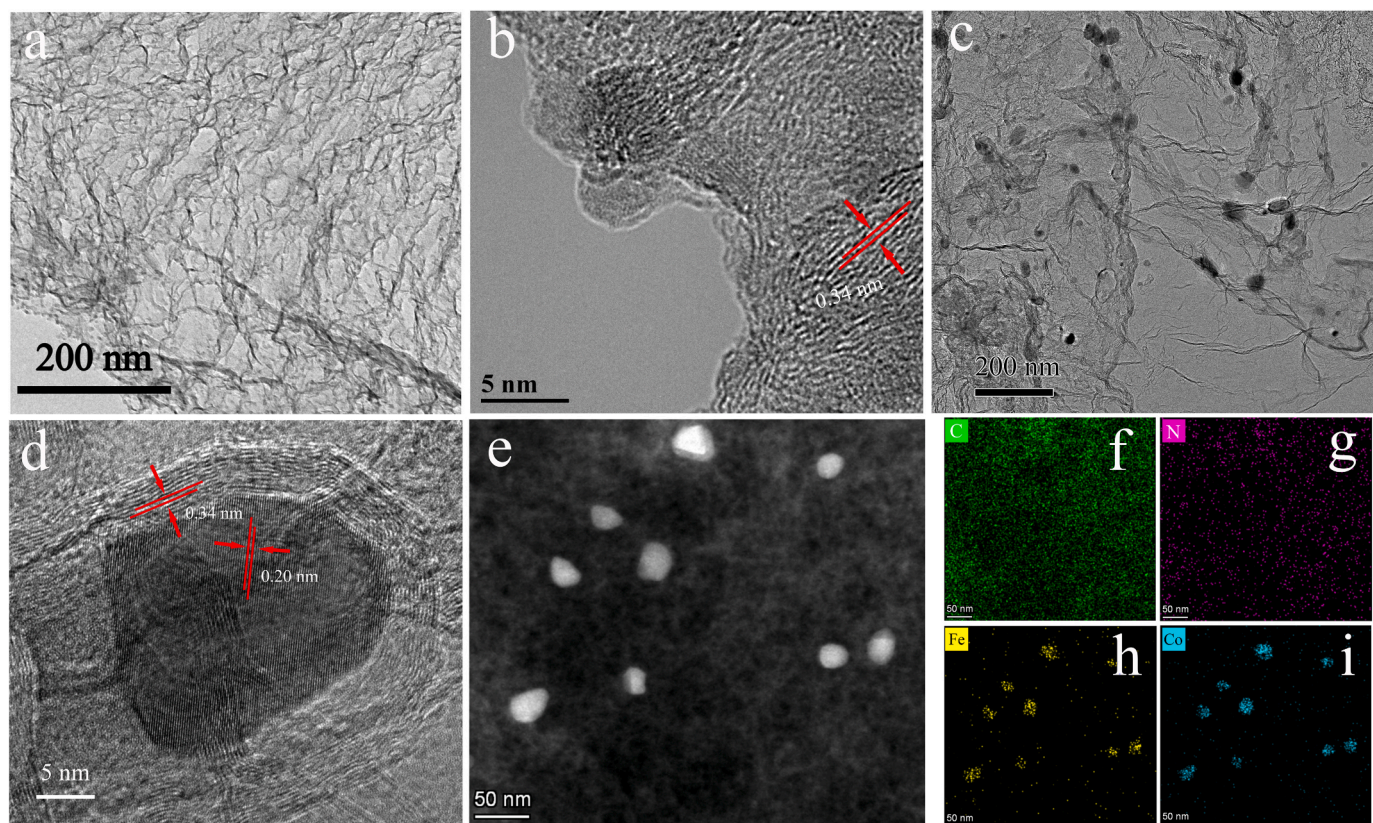


Fig. 1. Structure characterization of catalysts. (a) TEM image of NC, (b) HRTEM of NC, (c) TEM image of FeCo@NC, (d) HRTEM of FeCo@NC, and (e-i) TEM elemental mappings of FeCo@NC.

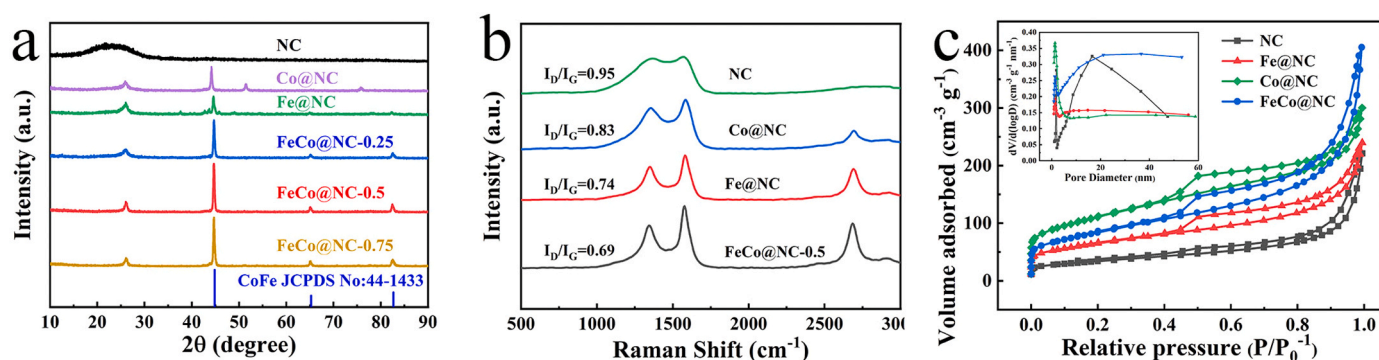


Fig. 2. (a) XRD patterns, (b) Raman spectrum, (c) N₂ adsorption-desorption isotherms and pore size distributions (Inset).

worth noting that, in the case of without metal doping, the surface area of NC was only 119.9 m² g⁻¹, which significantly increased when the metal component was introduced. The surface areas of Fe@NC, Co@NC and FeCo@NC were 1.91, 3.26 and 2.45 times than that of NC, respectively (Table S3). In addition, compared with Fe@NC or Co@NC, the introduction of bimetals further expanded pore size and pore volume, which was more conducive to the exposure of active center and facilitate the mass transfer of reactive species [35].

The surface chemical states of the functionalized carbon matrix of mono-metal or bimetallic nanoparticles were analyzed by high resolution X-ray photoelectron spectroscopy. As exhibited in Fig. 3b, the high-resolution C 1s spectra of various samples could be decomposed into three peaks of sp² graphitic-C (C-C, 284.8 eV), C-N (285.9 eV) and C-O bond (288.5 eV), which also confirmed the successful doping of N atoms into the carbon substrate [36]. High-resolution O 1s spectra could be decomposed into four peaks with binding energies of 529.9, 531.1, 532.1 and 533.6 eV, corresponding to lattice oxygen M=O (Fe=O or Co=O), C=O, C-C=O and O-C=O species, respectively [37–39]. In the high resolution N 1s spectrum (Fig. 3c and Table S3), the characteristic peaks at 397.9, 399.8, 400.9 and 402.4 eV belong to pyridine-N, pyrrole-N, graphic-N and oxide-N structures, respectively. Notably,

compared with the original NC, the relative content of pyridine-N increased significantly after the introduction of metal components, which may be due to the fact that pyridine-N is located at the edge of the graphite structure and easily combined with metal to form M-N_x as the catalytic active site [40]. In particular, Fe/Co-N_x sites are generally considered to be highly active for PMS activation [3,5]. In addition, after the introduction of metals, the pyridine-N peaks all shift significantly, revealing the electron interaction between metals and nitrogen atoms [36]. The characteristic peaks of the high resolution Fe 2p spectrum at 707.9 and 721.0 eV are related to the spin orbits of Fe⁰ 2p_{3/2} and Fe⁰ 2p_{1/2}. Similarly, the characteristic peaks of 778.4 and 793.7 eV in the Co 2p spectrum correspond to the Co⁰ 2p_{3/2} and Co⁰ 2p_{1/2} orbitals, and the presence of Fe⁰ and Co⁰ confirms the formation of FeCo alloys [36]. It was worth noting that the Fe⁰ peak has a negative shift after the formation of the alloy, which confirms the electronic structure change after the formation of alloy NPs [10]. And the charge redistribution around FeCo metal center may provide good surface energy, which is conducive to improving the overall rate of interfacial catalytic process [41].

Electrochemical impedance tests were conducted on the prepared NC, Fe@NC, Co@NC, and FeCo@NC to discover the electron-transfer

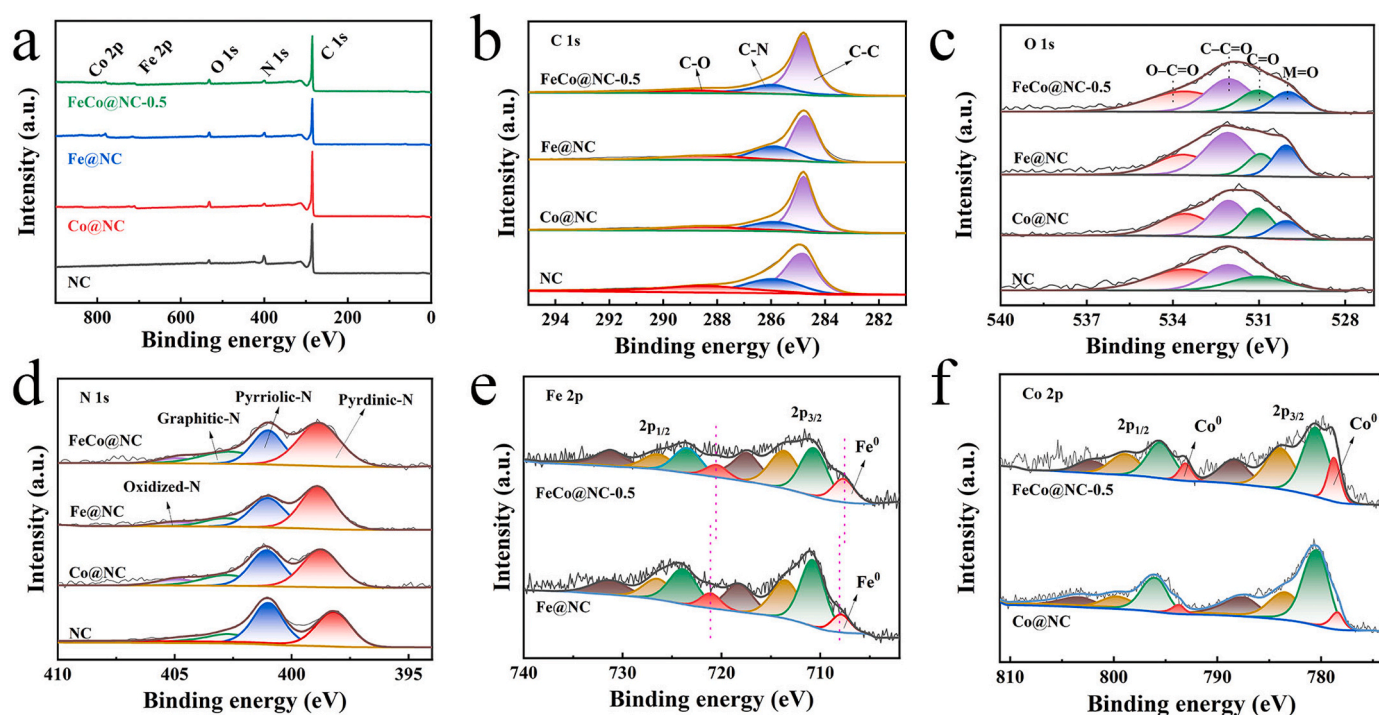


Fig. 3. (a) XPS full spectrum spectra of NC, Fe@NC, Co@NC and FeCo@NC, and High-resolution XPS spectrum of (b) C 1s, (c) O 1s, (d) N 1s, (e) Fe 2p and (f) Co 2p of as prepared catalysts.

kinetics (Fig. 4a). All impedance spectra consist of semicircles and slashes related to charge transfer resistance (R_{ct}) and diffusion characteristics (Z_w), respectively. R_s is the ohmic impedance obtained from the intercept of the high frequency region of the Z'_{real} axis [42]. It can be seen that the R_{ct} of Fe@NC and Co@NC is significantly lower than that of NC (Table S4), and the introduction of bimetallic elements further decreases the R_{ct} . The lower R_{ct} is more conducive to improving the catalytic activity and electron transfer kinetics [43]. This observation is consistent well with the previous Raman analysis, in which the I_D/I_G value of FeCo@NC is obviously lower than that of NC, Co@NC and Fe@NC, indicating the introduction of bimetals further improves the graphitization degree of catalyst. The higher graphitization is more conducive to the charge transfer within the catalyst [7], which reflects the synergistic effect between the bimetals.

The CV curves were measured in $K_3[Fe(CN)_6]$ to calculate the electroactive surface area (EASA) which reflects the actual surface active site of electrochemical reaction process [24]. As show in Fig. 4b and Table S4, the EASA of catalyst increases obviously after the introduction of Fe or Co. In addition, the EASA of FeCo@NC is 119.4 cm^2 , higher than that of Co@NC (104.4 cm^2) and Fe@NC (99.7 cm^2), indicating that the introduction of bimetallic alloys provides more reaction centers, which is beneficial to improving the catalytic activity.

To evaluate the catalytic activity and stability of the prepared catalysts, Tafel analysis was performed as shown in Fig. 4c, and the E_{corr} and i_{corr} of NC, Co@NC, Fe@NC and FeCo@NC are summarized in Table S4. It was found that the E_{corr} and i_{corr} of FeCo@NC was closer to zero compared to Co@NC and Fe@NC, indicating that the introduction of bimetallic elements made the catalysts more susceptible to corrosion. In addition, as important indicators for assessing charge transfer, Tafel slope can be used to indicate the charge transfer performance and electrocatalytic activity of catalyst [44,45], which can be obtained from the linear relationship region of the Tafel plot, as shown in Fig. S3. The Tafel slope of FeCo@NC is significantly lower (Table S4) (when the overpotential is the x-coordinate, the slope should be reciprocal according to the Tafel equation), indicating that FeCo@NC has more reaction sites and faster catalytic reaction kinetics [46].

3.2. Evaluation of catalytic activity

The influence of various catalysts on the coupling activation of PMS were explored by CBZ degradation experiments. Firstly, the effects of different Fe/Co ratios on the catalytic removal were conducted. The removal efficiency of CBZ by FeCo@NC-x modified carbon felt cathode is higher than that of Fe@NC and Co@NC (Fig. 5a), and the best ratio of Fe to Co was 1:1, in which CBZ can be completely degraded within 45 min. The apparent kinetic constant k of FeCo@NC is 0.0811 min^{-1} , which is 5.68 times that of Fe@NC and 3.74 times that of Co@NC (Fig. 5b). This probably because the synergies of bimetal to promote the activation of PMS, thus promoting the overall degradation of

carbamazepine. In addition, the metal leaching amount (Fe 0.1273 mg L^{-1} and Co 0.0418 mg L^{-1} for FeCo@NC) reduced after the introduction of complementary metal elements (Fig. 5b), which may be due to the formation of FeCo-N coordination structure which increases the stability of the catalyst [11]. Furthermore, the influence of metal content (the precursor of Fe and Co was 0.25, 0.5 or 0.75 mmol) was discussed on the basis of 1:1 Fe/Co ratio (Fig. 5c). It was found that metal content had a significant effect on the degradation efficiency and the metal leaching increased with the increase of precursors volume (Fig. 5d). The FeCo@NC system had the highest degradation efficiency, and the k value was 5.84 times that of NC (Fig. S4).

Combined the XPS analysis of various catalysts with different Fe and Co ratios (FeCo = 2:1, 1:1, 1:2) or different metal content (the precursor of Fe and Co was 0.25 or 0.75 mmol), it is found that there are more sp^2 -hybridized C-C moieties, O-C=O and M=O groups in FeCo@NC (Table S5) than in Co@NC and Fe@NC. And the apparent reaction rate constant of CBZ degradation increased monotonically with the content of C-C moieties ($r^2 = 0.937$), and algebraic sum of O-C=O and M=O group ($r^2 = 0.942$) [7], while significantly negatively correlated with the relative contents of C-O ($r^2 = 0.966$, Fig. 6(a-b)). Duan et al. suggested that the intact sp^2 hybrid carbonaceous networks can stimulate the asymmetric O-O bond of PMS molecules ($HO-SO_4^*$) to generate $\cdot OH$ and $SO_4^{\cdot -}$ [47], thus more available sp^2 -hybridized C-C moieties may endow the as fabricated catalysts with improved catalytic activity. On the other hand, PMS molecules are more liable to be adsorbed on the positively charged C atom in O-C=O [37], and the M=O group (Fe=O or Co=O) has been demonstrated to be the major activation site of PMS [48,49], thereby more available O-C=O and M=O components promote the activation of PMS to produce more ROS, and then accelerate the degradation of CBZ.

In order to better understand the influence of different metal active centers and functional groups on the activation of PMS, density functional theory (DFT) calculations were used to study the activation properties of PMS. Interestingly, catalysts exhibit significant difference in activation performance of PMS with or without surface functional groups, as shown in Fig. 6c. The PMS adsorbed on the active site receives an electron from the metal center, triggering the O-O bond to break, which results in the production of radicals and hypervalent metal sites [50]. FeCo@NC exhibits more reaction free energy drop than Co@NC and Fe@NC, indicating that the establishment of bimetallic active sites can reduce the energy barrier of O-O bond breakage of PMS [11], and is more conducive to the activation of PMS to produce $SO_4^{\cdot -}$ than single-component metals. These results are in good agreement with the degradation experimental results. When more O-C=O component is added to the optimized FeCo@NC model (Fig. S5), the maximum total energy released during the reaction significantly increased, further indicating that the corresponding functional group components can promote the activation of PMS.

The above results suggest that the faster charge transfer (synergistic

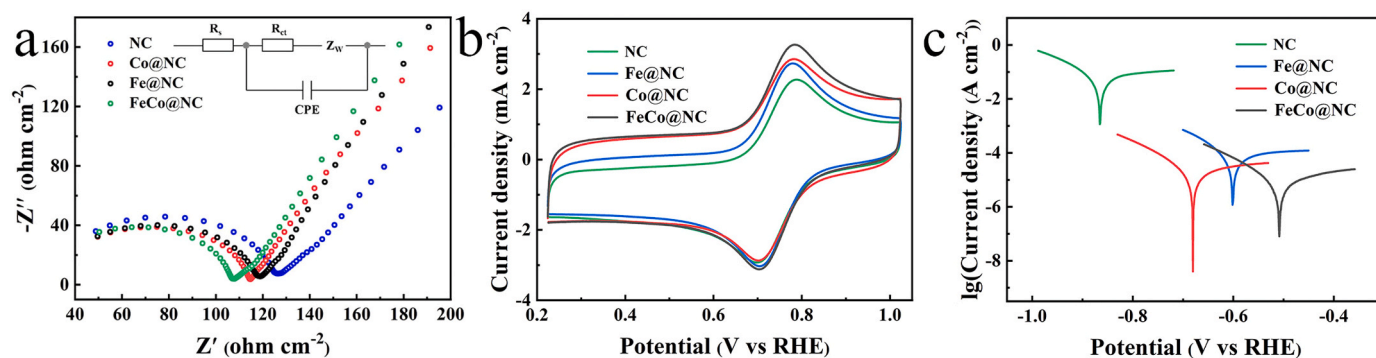


Fig. 4. Electrochemical characterizations of as-prepared catalysts: (a) Nyquist plots, (b) CV curve in 1 M KCl containing 10 mM $K_3[Fe(CN)_6]$, scan rate = 0.1 Vs^{-1} , (c) Tafel polarization curve, scan rate = 0.01 Vs^{-1} .

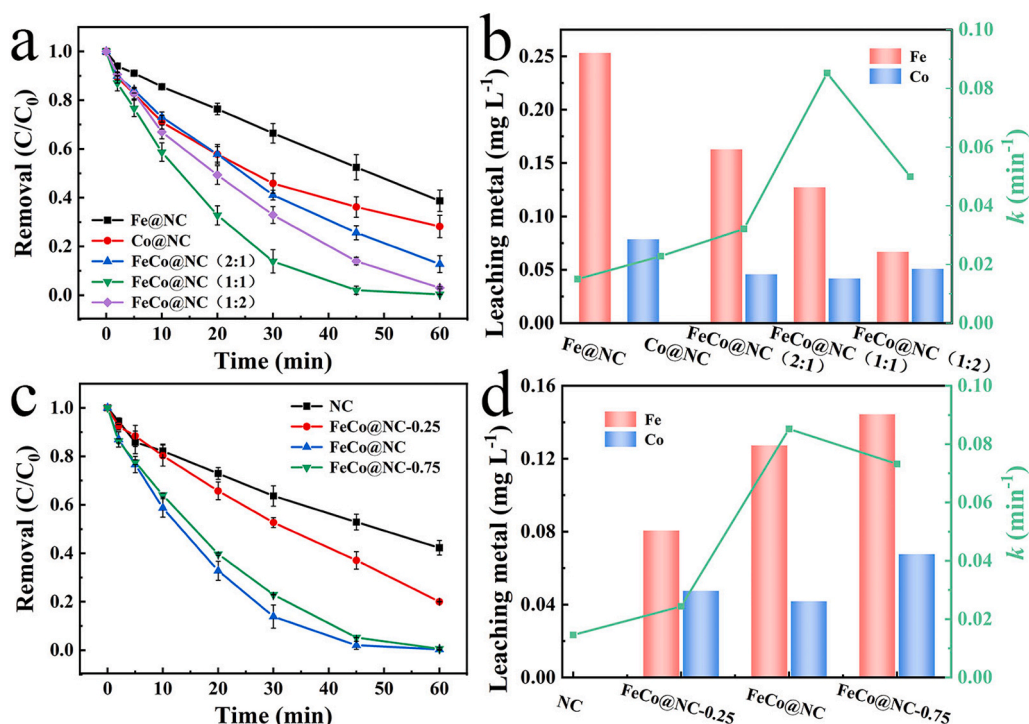


Fig. 5. (a-b) The CBZ degradation performance, leaching metal concentration and k value of various catalysts with different proportion of Fe:Co = 1:0, 0:1, 2:1, 1:1 and 1:2, (c-d) The influence of different metal contents on CBZ degradation, leaching metal concentration and k value. [CBZ]₀ = 10 ppm, [PMS]₀ = 1.5 mM, [Na₂SO₄]₀ = 50 mM, pH₀ = 7.0, current density = 1.67 mA cm⁻².

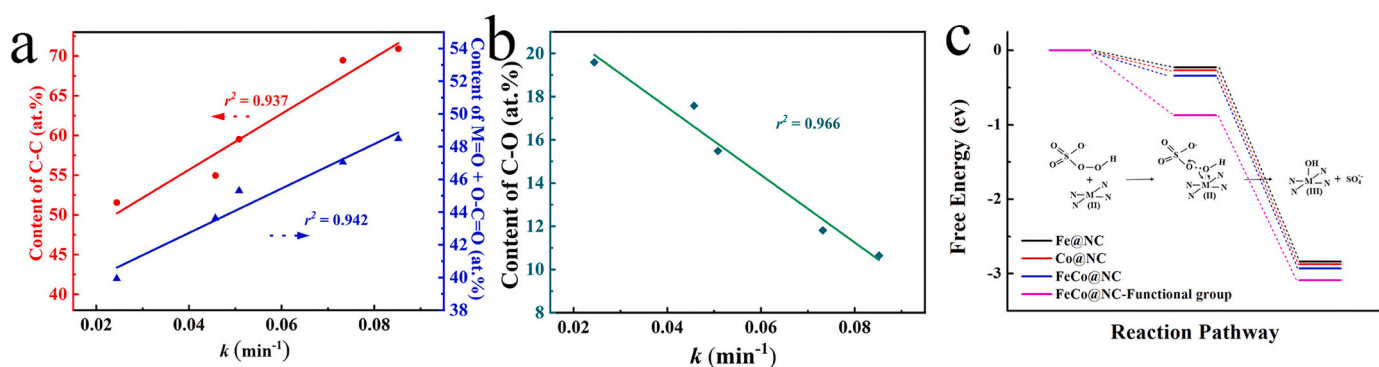


Fig. 6. The apparent CBZ removal rates as functions of the content of C-C, algebraic sum of O=C=O and M=O (a), and C-O (b); Energy diagrams and reaction pathway during the activation of PMS by Fe@NC, Co@NC, FeCo@NC and FeCo@NC with more functional groups (c).

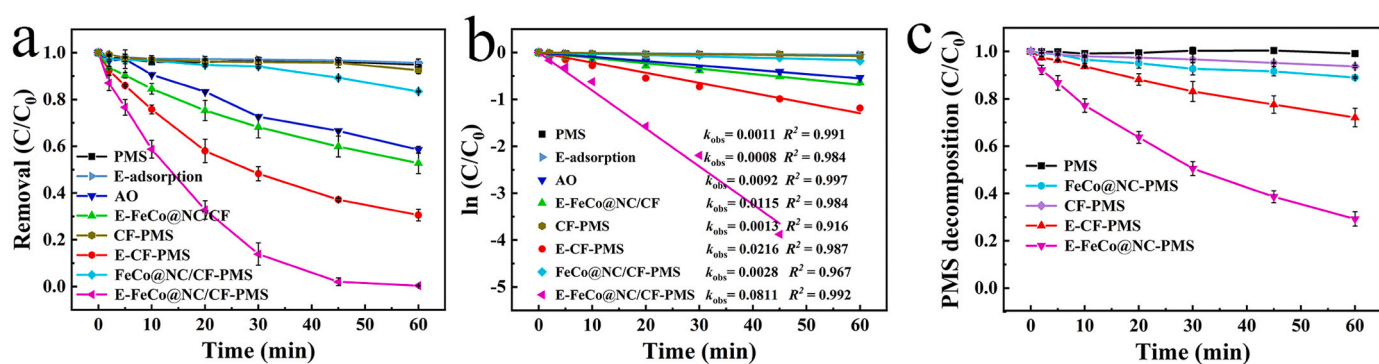


Fig. 7. Comparison of the CBZ degradation performance (a), k value (b) and PMS consumption (c) in different oxidation processes. Experimental conditions: [CBZ]₀ = 10 ppm, [PMS]₀ = 1.5 mM, [Na₂SO₄]₀ = 50 mM, pH₀ = 7.0, current density = 1.67 mA cm⁻².

effect between bimetals), the coexistence of graphitic carbon components and oxygen-containing functional group components such as $\text{O}=\text{C}=\text{O}$ and $\text{M}=\text{O}$ are related to improving the removal performance of CBZ.

3.3. Synergistic effect of electro-activation and catalytic-activation for PMS

The degradation of CBZ in different process were investigated to evaluate the synergistic effect of electro-activation and catalytic-activation for PMS.

Electro-adsorption (E-adsorption), anodic oxidation (AO) and FeCo@NC/CF cathode Fenton-like reaction (E- FeCo@NC/CF) were carried out at a current density of 1.67 mA cm^{-2} . As shown in Fig. 7a, the E-adsorption could remove 3.5% of CBZ, while the removal of CBZ by AO or E- FeCo@NC/CF process is 41.49% or 47.24%, respectively, which can be attributed to the $\cdot\text{OH}$ formed on the DSA anode surface and the Fenton-like reaction on cathode [51]. It is well known that carbon felt cathode can produce H_2O_2 through the 2e^- oxygen reduction pathway, so the H_2O_2 productions in the CF and FeCo@NC/CF cathode systems were monitored as shown in Fig. S6. In the CF system, the H_2O_2 production increased in the first 20 min and then decreased gradually, with the highest H_2O_2 concentration of 8.9 mg L^{-1} . This is because the electrochemical degradation experiments were performed without aeration, and the dissolved oxygen in the solution was consumed in the first 20 min, while the oxygen generated by the anodic oxidation afterwards was not sufficient to ensure the H_2O_2 production at the cathode. In contrast, the H_2O_2 yield in the E- FeCo@NC/CF system was significantly lower, only 1.8 mg L^{-1} at 60 min. The lower H_2O_2 yield may be due to the cover of the CF surface active site or the consumption of H_2O_2 by the Fenton-like reaction on the FeCo@NC/CF . Therefore, the steady-state $\cdot\text{OH}$ concentrations $[\cdot\text{OH}]_{\text{ss}}$ in the AO and E- FeCo@NC/CF systems were calculated using NB as a probe through Eq. 5 as shown in Fig. S7. The $[\cdot\text{OH}]_{\text{ss}}$ in the E- FeCo@NC/CF system was calculated to be $6.4 \times 10^{-13} \text{ M}$, which is slightly higher than that in the AO system ($5.9 \times 10^{-13} \text{ M}$), indicating that the restricted H_2O_2 production prevents the Fenton-like reaction from occurring on the cathode surface. In addition, the CBZ removal efficiency of E- FeCo@NC/CF only increased by 5.75% compared with AO process, indicating that the Fenton-like reaction on the cathode has no significant effect in the E- FeCo@NC/CF system.

The removal efficiency of CBZ by PMS alone was almost negligible, indicating that the oxidation capacity of PMS itself was not enough to degrade CBZ. In addition, the activation of PMS by FeCo@NC/CF (FeCo@NC/CF-PMS) could only remove 35% of CBZ when no current was applied. The surface wettability of CF and FeCo@NC/CF were analyzed through contact angle measurement. As shown in Fig. S8, the contact angles of CF and FeCo@NC/CF were 141.56° and 127.81° respectively. The low CBZ removal efficiency may due to the hydrophobic properties of the CF surface, which may impede the mass transfer between the FeCo@NC catalyst coated on CF and the related species in solution. It can also be seen from Fig. 7c that the consumption of PMS in the FeCo@NC/CF system is only 11.1%, indicating that the activation of PMS by FeCo@NC/CF is hindered by the mass transfer due to a hydrophobic interface.

Importantly, when no current was added, the CBZ removal was only 7.5%, and only 6.3% of the PMS was consumed (Fig. 7a,c) when the PMS was activated by CF (CF-PMS), indicating that the original CF has a weak activation ability for PMS in the case of no electricity. However, when a current density of 1.67 mA cm^{-2} was applied, the activation of PMS by CF cathode could removal 69.47% of CBZ (E-CF-PMS), and the consumption of PMS also increased to 27.9%, indicating that PMS was electro-activated on the CF cathode surface [28,52]. Moreover, the CBZ removal was significantly improved by the E- FeCo@NC/CF-PMS system. The target contaminant was almost completely removed within 45 min, indicating that there was a synergistic effect between electric activation

and FeCo@NC/CF catalysis for PMS. Interestingly, the wettability of CF surface changed significantly after electric field was applied. As shown in supplementary Video 1, water droplets could only accumulate on the FeCo@NC/CF surface but could not penetrate after the FeCo@NC/CF-PMS process, while immediately infiltrated into the FeCo@NC/CF after the E- FeCo@NC/CF-PMS process. This may be the electrowetting caused by the application of external voltage between the solid-liquid interface [53]. The compatibility of most hydrophilic solute to water comes from attractive interactions between ionized or polar groups of the solute with dipoles and quadrupoles of water molecules [54]. A similar effect can be produced by applying an external voltage to the solid/liquid interface, which reduces the interface free energy because water dipoles interact well with the external field [53]. Consequently, the solution can flow in the three-dimensional porous network space of CF after an electric field is applied, which can accelerate the mass transfer between the key reactants and the active site on the electrode surface [55]. What is noteworthy is that the surface of FeCo@NC/CF returned to the hydrophobic state after the residual water evaporated (Video 2), suggesting that the cathode can switch between dry and wet states due to the condensation and evaporation of water inside the pores by applying an electric potential [56], which further demonstrates the critical role of electric field in the E- FeCo@NC/CF-PMS process.

According to the above analysis, the synergistic effect of electrochemical activation and catalytic activation for PMS can contribute to the in situ activation of PMS through the direct electron transfer on the cathode surface [52] and the enhanced mass transfer between FeCo@NC/CF and solution. The synergistic factor (S) was calculated with Eq. (2) to quantify the interaction degree [26,27]. The high $S_{\text{E-CF-PMS}}$ (2.09) was due to the formation of ROS by the electrochemical activation of PMS, which accelerated the kinetics of CBZ degradation. $S_{\text{FeCo@NC/CF-PMS}}$ was 1.47 due to the activation of PMS by FeCo@NC catalyst. Importantly, the $S_{\text{E-FeCo@NC/CF-PMS}}$ was 3.49, much higher than $S_{\text{E-CF-PMS}}$ and $S_{\text{FeCo@NC/CF-PMS}}$. These results indicate a good synergistic activation of PMS by electro-activation and FeCo@NC catalysis. In addition, the electric field could also promote the redox cycle of active species ($\text{Fe}^{2+}/\text{Fe}^{3+}$, $\text{Co}^{2+}/\text{Co}^{3+}$) in FeCo@NC , and improve the cycle stability of FeCo@NC/CF , which will be described later.

3.4. Parameters optimization

The effect of current density on the synergistic effect in the E- FeCo@NC/CF-PMS system was studied based on the above analysis. As shown in Fig. 8a, the removal efficiency of CBZ increased to a maximum value as the current density increased from 0.83 to 1.67 mA cm^{-2} (the DC supply voltage is -1.4 V with a -0.314 V potentials (vs. Ag/AgCl) of FeCo@NC/CF cathode), and then decreased. This is because the increased current promoted the electro-activation of PMS through the increased charge transfer [52], while excessively high electric field caused obvious hydrogen evolution reaction. H^+ would compete with HSO_5^- for electrons [29]. In addition, the high electric field could reduce the contact between HSO_5^- and the cathode interface due to electric field resistance [57]. Previous studies also shown that applying different electrochemical perturbations to the electrode results in changes in the concentration distribution of reactive species in the Nernst layer on the electrode surface [58,59]. Therefore, based on the above experimental results, the optimal applied current density was 1.67 mA cm^{-2} .

The PMS dosage directly affects the removal reaction of organic (Fig. 8b). The degradation of CBZ obviously increased with the increasing of PMS dosage, which is due to the sufficient reaction between an increasing number of PMS and quantitative active sites on FeCo@NC/CF cathode. However, the CBZ removal efficiency did not continue to increase but slightly decreased when the PMS dosage increased to 2.0 mM . Because the low PMS concentration is the determinant when the active site is sufficient, 1.5 mM of PMS fully occupies the reactive site of FeCo@NC/CF cathode, which promotes the rapid

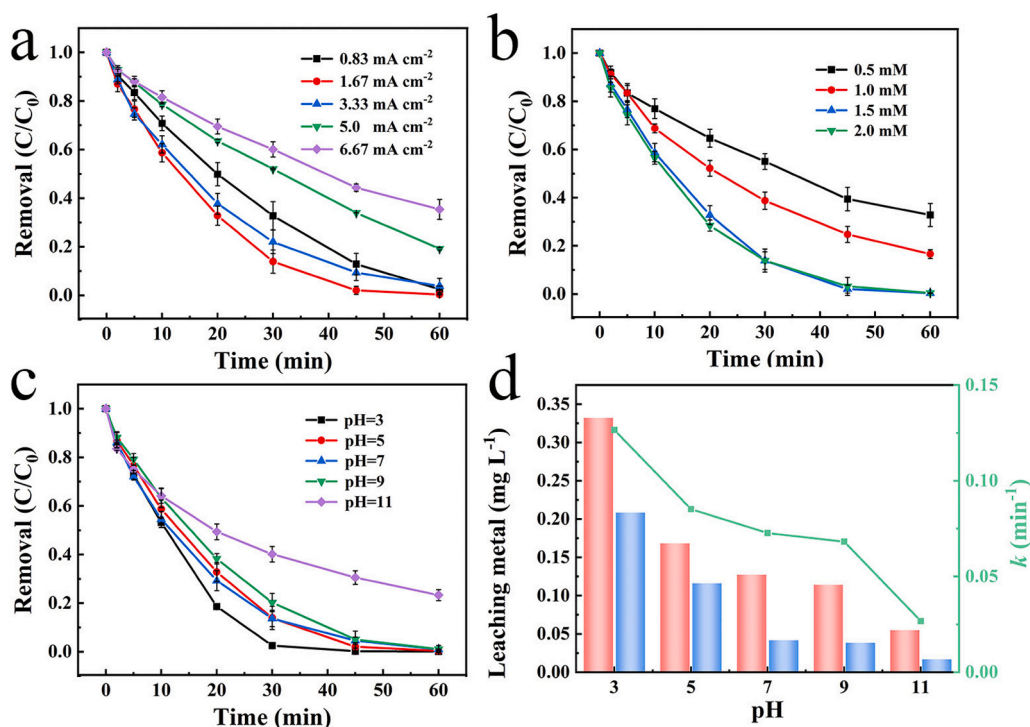


Fig. 8. Effect of (a) current density, (b) PMS dosage and (c) pH on the degradation of CBZ, and (d) the leaching metal concentration and k value at different pH. Experimental conditions: $[CBZ]_0 = 10$ ppm, $[PMS]_0 = 1.5$ mM, $[Na_2SO_4]_0 = 50$ mM, $pH_0 = 7.0$, current density = 1.67 mA cm⁻².

reaction of PMS to generate sufficient ROS to degraded CBZ [29]. However, too much PMS generates more reactive species, which tend to react with each other to produce less oxidizing species through radical

chain reaction [60]. In addition, excess PMS reacts directly with the reactive species, thus quenching the generated radicals through the reactions of Eqs. (12, 13) and leading to a reduction in CBZ removal

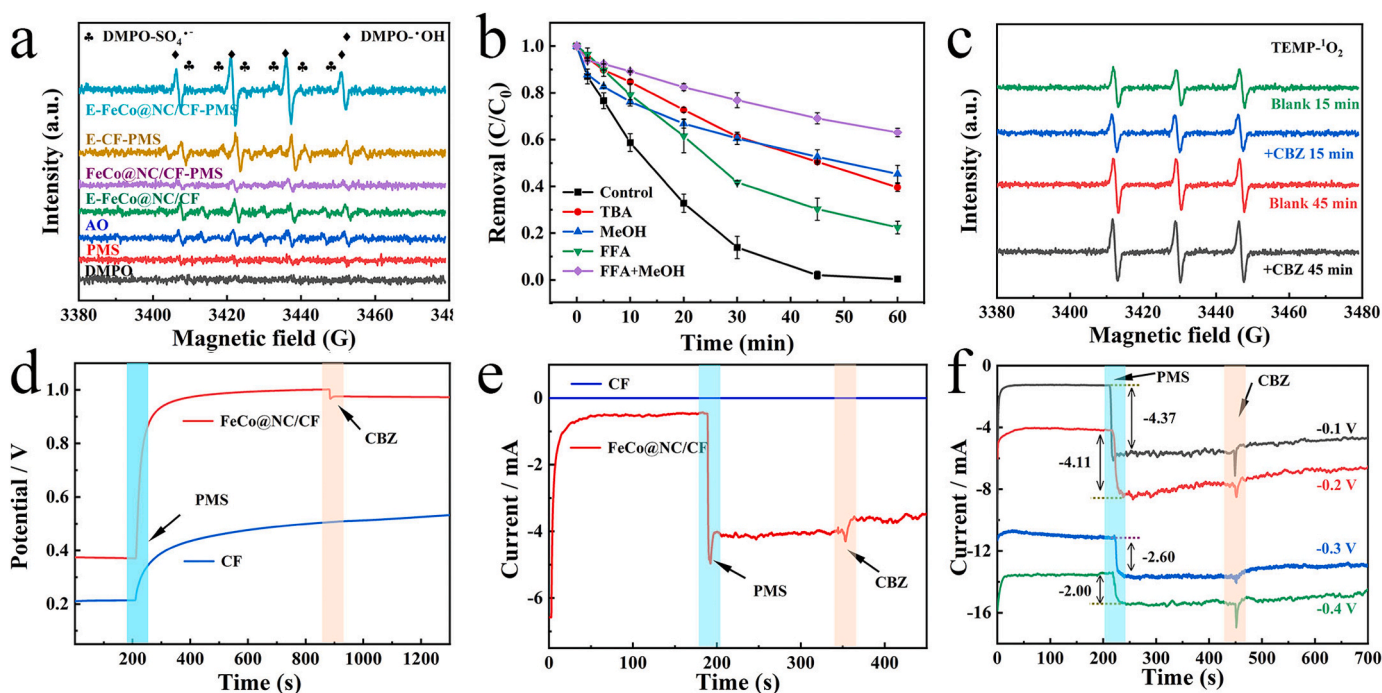
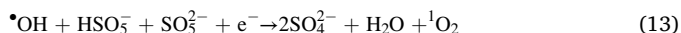


Fig. 9. (a) EPR spectra of DMPO·OH in different processes, reaction condition: $[PMS]_0 = 1.5$ mM, $[Na_2SO_4]_0 = 50$ mM, $pH_0 = 7.0$, current density = 1.67 mA cm⁻², (b) CBZ removal with the addition of different scavengers in E-FeCo@NC/CF-PMS process, reaction condition: $[CBZ]_0 = 10$ ppm, $[PMS]_0 = 1.5$ mM, $[Na_2SO_4]_0 = 50$ mM, $pH_0 = 7.0$, current density = 1.67 mA cm⁻², $[TBA]_0 = 10$ mM, $[MeOH]_0 = 500$ mM, $[FFA]_0 = 5$ mM, (c) EPR spectra of TEMP·O₂ with or without CBZ in E-FeCo@NC/CF-PMS process, (d) open-circuit potential curves of FeCo@NC/CF electrode with the addition of PMS and CBZ, (e) Amperometric $i-t$ curves upon the addition of PMS and CBZ with an initial potential of 0 V (Ref. Ag/AgCl), and (f) Amperometric $i-t$ curves at different cathode working potentials.

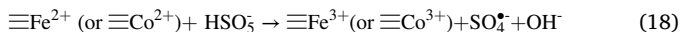
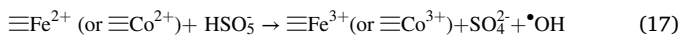
efficiency [22].

The effect of initial pH on CBZ removal in E-FeCo@NC/CF/PMS system was also studied. As shown in Fig. 8c, almost all CBZ can be completely removed within 60 min at pH 3.0–9.0, indicating that the E-FeCo@NC/CF-PMS process can be used to treat wastewater within a wide pH range. The metal leaching amount decreased with the increase of pH and was lower than the values reported in others literature [7,38,61,62], indicating that the catalyst had excellent stability, which could be attributed to the protective effect of the external graphite shell on the internal alloy.



3.5. Mechanism discussion

In order to elucidate the possible ROS in the E-FeCo@NC/CF-PMS process, the EPR analysis was performed with 5,5-Dimethyl-1-pyrroline N-oxide (DMPO) as a spin trapping agent. As shown in Fig. 9a, the weak DMPO- $\bullet\text{OH}$ signal was observed in the AO and E-FeCo@NC/CF processes, which could be attributed to the surface hydroxyl radical on the anode or the cathodic Fenton reaction in the E-FeCo@NC/CF process. In addition, no significant signal peaks were observed in the presence of PMS alone, while the E-CF-PMS system produced a significant DMPO- $\bullet\text{OH}$ signal, further proving that the hydroxyl radical can be generated from the activation of PMS by electrochemical activation. Interestingly, the DMPO- $\bullet\text{OH}$ signal in the E-FeCo@NC/CF-PMS process was significantly stronger than that in E-CF-PMS and FeCo@NC/CF-PMS, and a similar phenomenon occurred when 2,2,6,6-tetramethyl-4-piperidinol (TEMP) was used as a spin trapping agent for ${}^1\text{O}_2$ (Fig. S9), which further proved the synergistic activation of PMS by electricity and FeCo@NC/CF catalyst, and this is most probably the reason that the fast degradation of CBZ in the E-FeCo@NC/CF-PMS process. Based on the above analysis, the $\bullet\text{OH}$ can be generated via Eqs.(14–18). It was worth noting that the DMPO- $\bullet\text{OH}$ signal intensity gradually increased only in the first 15 min of reaction and then gradually decreased in the E-CF-PMS process (Fig. S10), whereas it kept increasing during the whole reaction process (60 min) in the E-FeCo@NC/CF-PMS process. These results indicate that the continuously generated hydroxyl radical is responsible for the synergistic effect of electrochemical activation and FeCo@NC catalysis.



Radical scavenging experiments were performed in the E-FeCo@NC/CF-PMS process to further elucidate the degradation mechanism. Methanol (MeOH) was used as a scavenger for both $\bullet\text{OH}$ ($k = 2.5 \times 10^7 \text{ M}^{-1}\text{s}^{-1}$) and $\text{SO}_4^{\bullet-}$ ($k = 9.7 \times 10^8 \text{ M}^{-1}\text{s}^{-1}$). Tertiary butanol (TBA), as the trapping agent of $\bullet\text{OH}$ ($k = 3.8\text{--}7.6 \times 10^8 \text{ M}^{-1}\text{s}^{-1}$), is relatively insensitive to $\text{SO}_4^{\bullet-}$ ($k = 4.0\text{--}9.1 \times 10^5 \text{ M}^{-1}\text{s}^{-1}$). As shown in Fig. 9b, the degradation of CBZ was significantly inhibited after the addition of MeOH or TBA, and the inhibitory effects of MeOH and TBA were almost the same, indicating that the most radical species was $\bullet\text{OH}$ rather than $\text{SO}_4^{\bullet-}$. This result was consistent with the EPR analysis shown in Fig. 9a, and there was no obvious signal of DMPO- $\text{SO}_4^{\bullet-}$, which probably due to

the reaction between $\text{SO}_4^{\bullet-}$ and H_2O or OH^- to generate $\bullet\text{OH}$ via Eqs. (19, 20) [22].

Although the addition of MeOH or TBA inhibited the removal of CBZ to a certain extent, about 56% of CBZ were removed, so there are still other ROS in the system contributing to the removal of CBZ. Recently, nonradical mediated activation of PMS has been reported in different catalysis systems, such as ${}^1\text{O}_2$ [63], hyperferric oxygen complexes [48, 64] or electron transfer process (ETP) [7,15].

The contribution of ${}^1\text{O}_2$ was investigated through selective quenching experiment. It is considered that the commonly used ${}^1\text{O}_2$ quenchers (such as histidine) may inevitably react with PMS, resulting in reduced removal of target contaminants [65]. Therefore, we screened three ${}^1\text{O}_2$ quench agents reported in literatures, such as histidine, furfuryl alcohol and TEMP [3,61,64], and then monitored the PMS consumption when they react with PMS separately. As shown in Fig. S11, different concentrations of quenching agent measurements showed different levels of PMS consumption, and FFA consumed the least PMS, accounting for only 0.62% of PMS at 5 mM. Therefore, FFA was chosen as the quench agent for ${}^1\text{O}_2$. As shown in Fig. 9b, after adding FFA to the E-FeCo@NC/CF-PMS system, the removal of CBZ decreased to 77.6%, indicating that ${}^1\text{O}_2$ was one of the active species of CBZ degradation. Moreover, EPR detection was further carried out in the system with or without CBZ (Fig. 9c). Interestingly, the signal intensity of characteristic peak corresponding to ${}^1\text{O}_2$ did not decrease in the reaction process with the addition of CBZ. This seems to imply that no ${}^1\text{O}_2$ is consumed during the process of CBZ removal. However, the CBZ removal efficiency decreased to 77.6% when FFA was chosen as the quenching agent for ${}^1\text{O}_2$, which may be because FFA competes with CBZ to consume $\bullet\text{OH}$. The second-order rate constant of FFA and $\bullet\text{OH}$ ($k_{\text{FFA},\bullet\text{OH}} = 1.5 \times 10^{10} \text{ M}^{-1} \text{ s}^{-1}$) is higher than that of CBZ and $\bullet\text{OH}$ ($k_{\text{CBZ},\bullet\text{OH}} = 8.8 \times 10^9 \text{ M}^{-1} \text{ s}^{-1}$) [32,49], therefore FFA is more readily oxidized than CBZ, which depletes the ROS produced in the E-FeCo@NC/CF-PMS process. The contradiction between the capture experiment and EPR analysis prompted us to explore the contribution of ${}^1\text{O}_2$ to the degradation of CBZ through probe experiment that will be introduced later.

Recently, high-valent metal oxygen complex such as Fe(IV)/Fe(V) and Co(IV) has been proved as a possible reactive species in PMS process [48,64]. To explore whether the high-valent metal oxygen complexes were produced in E-FeCo@NC/CF-PMS process, a selective scavenger dimethyl sulfoxide (DMSO) was used to quench the CBZ degradation, as DMSO can consume the high-valent metal oxygen reactive site [7]. As shown in Fig. S12, the removal efficiency of CBZ was only reduced by 7.4%. In addition, methyl phenyl sulfoxide (PMSO) was used to further prove the above conclusion based on the fact that PMSO can be oxidized by high-valent metals or ${}^1\text{O}_2$ to form the byproduct of PMSO₂ through an oxygen atom transfer reaction [66]. The consumption of PMSO and generation PMSO₂ in E-FeCo@NC/CF-PMS process were almost the same compared with those in E-CF-PMS process (Fig. S13). The above experiment results indicated that the high-valent metal oxygen species was absent in the E-FeCo@NC/CF-PMS process. However, it was found that the degradation of CBZ was almost completely inhibited when KI was used as a surface reaction inhibitor (Fig.S12). Although KI can also be used to quench $\bullet\text{OH}$ in solution, the degradation inhibition of CBZ is significantly stronger when KI was used as the inhibition than that of TBA (Fig. 9b), indicating that there may be an important surface reaction mechanism in the system that contributed to the removal of CBZ.

On the other hand, the possible electron-transfer pathway (ETP) in the process was detected through open circuit potential test and current-time curve. As shown in Fig. 9d, when the FeCo@NC/CF was used as cathode, the initial potential of FeCo@NC was $\sim 0.37 \text{ V}$, which rose to $\sim 1.0 \text{ V}$ after the addition of PMS. It has been reported that PMS can be attached to the active site to form a metastable intermediate (FeCo@NC-PMS*), which has a high oxidation potential [7,15]. After the addition of CBZ in this study, the potential decreased significantly, indicating that FeCo@NC-PMS* extracted electrons from pollutants, thus triggering

ETP, and ultimately reduced the potential of FeCo@NC-PMS*. Furthermore, the formation of FeCo@NC-PMS* and ETP path of CBZ degradation can also be verified through the linear relation region of the Tafel curve shown in Fig. S14. When PMS is applied, the slope of the linearly correlated region fitting of the polarization curve is higher, which further indicates that a fast kinetic process related to PMS adsorption/activation occurs on the FeCo@NC surface [67]. Notably, the slope of the fitted curve increases further as CBZ is added, indicating more intense electron transport on the catalyst surface. The above analysis demonstrated the formation of FeCo@NC-PMS* and the subsequent degradation of CBZ via ETP pathway.

However, only a small potential increase of CF cathode was found after the addition of PMS, and the potential remained stable after the dosage of CBZ (Fig. 9d). These results indicated the critical role of FeCo@NC catalyst in ETP. The existence of ETP degradation pathway was further verified by the *i*-*t* curve (Fig. 9e). Specifically, when the FeCo@NC/CF was used as cathode, the rapid formation of surface-bound PMS* and the consumption associated with contaminants were confirmed by a sudden current drop (ΔI_{+PMS}) after the addition of PMS at an initial potential of 0 V (vs Ag/AgCl) and a partial current rebound (ΔI_{+CBZ}) after the dose of CBZ when the FeCo@NC/CF was used as cathode [26,68]. However, there was no significant fluctuation in the current curve after the dosage of PMS or CBZ when the CF was cathode. These results indicate that the FeCo@NC catalysis rather than electrochemical activation is responsible for the ETP.

In general, the activation process of PMS based on heterogeneous metal catalysts first involves the adsorption of PMS at the catalytic active site and the subsequent activation of PMS to produce reactive species [62]. Considering that high cathode electric field would hinder the adsorption of HSO₅⁻ to some extent, the *i*-*t* curve at different cathode potentials of -0.1 V to -0.4 V (vs Ag/AgCl) was tested. As shown in Fig. 9 f, the initial platform region corresponds to the current response caused by electron transfer in the electrochemical circuit formed by the cathode and the electrolyte at different potentials. The initial current response also increases with the increase of the cathode applied potential. The enhanced current response appeared in all curves with the dose of PMS, indicating that the surface binding PMS* can be formed at all different cathode potentials (ΔI_{+PMS} decreased with the increase of cathode potential, proving that the repulsion of PMS molecules on the electrode surface increased with the increase of cathode potential), which accelerates the number of electrons transferred by the cathode. It is worth noting that a new response platform appeared and the current response is slightly weaker after the dose of CBZ at all applied potentials, which is possibly because the formed FeCo@NC/CF-PMS* complex directly grabs electrons from CBZ, reducing the number of electrons obtained from the cathode, and resulting in a slightly smaller current response.

The degradation intermediates in the E-FeCo@NC/CF-PMS system were detected by LC-MS (Table S7), and the possible degradation pathways of CBZ were deduced accordingly, as shown in Fig. S15. In general, the alkene double bond in CBZ is more susceptible to ROS attack due to the high frontier electron density (FED). Furthermore, the degradation product P253 (10,11-epoxycarbamazepine) was detected in the mass spectrum at *m/z* = 253 and was more abundant than the other degradation products, suggesting that P253 was generated due to ROS attack on the olefinic double bond of central heterocyclic ring of CBZ and may be a precursor to other intermediates [69]. After that, P253 is further oxidized through four pathways. First, P253 was hydrolyzed to form P271 (dihydroxy carbamazepine), which underwent heterocyclic ring open process to form the dialdehyde compound P269 (N,N-bis (2-carboxyphenyl)urea) [69]. Also P253 can be directly converted to P269 through C-C bond breakage [70]. Afterwards, P269 underwent a ring contraction reaction and intramolecular cyclization via electrophilic aromatic substitution to produce P267, after which P267 formed P224 by acetyl cleavage [71], and P224 continued to undergo aldol cleavage to produce P196. In the third pathway, P253 was converted to

P208 by ring contraction as well as amide deletion. In addition, P253 can also undergo a simple ring contraction to produce P210, which is usually occurs by a pinacol-type rearrangement [72]. Further oxidation of P210 led to breakage of the aldehyde group and production of P180 [73], which was further converted to form P196 [74]. Finally, these intermediates underwent ring cleavage and were converted to small molecules as a result of ROS attack.

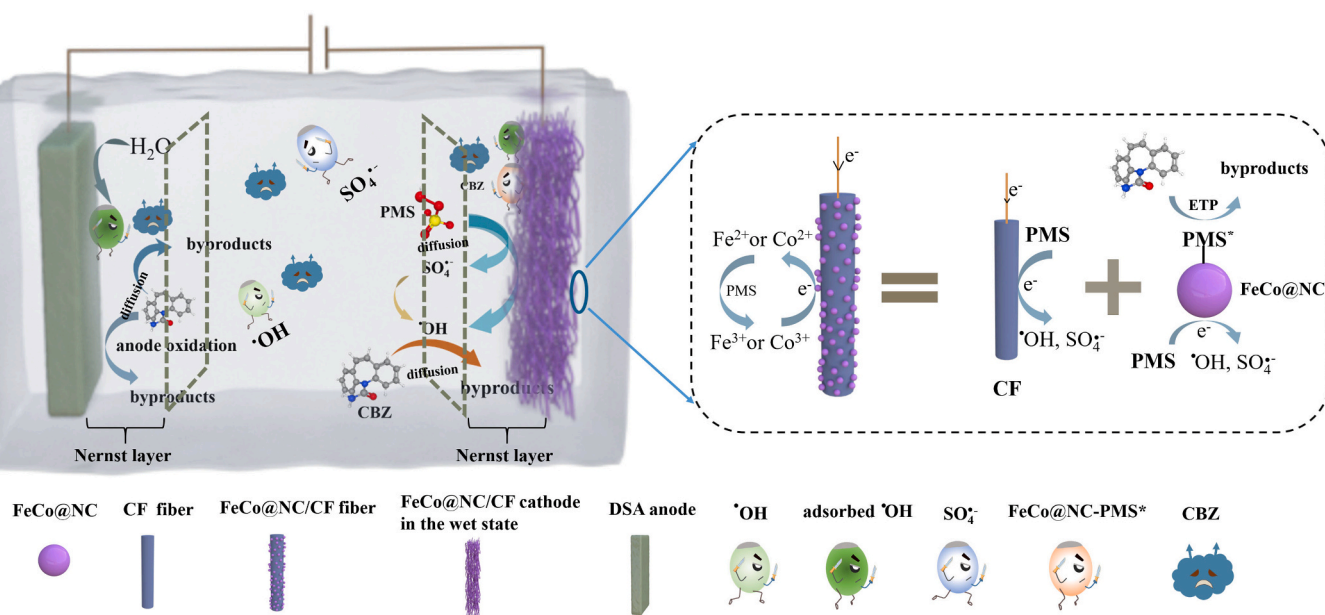
In addition, it is important to understand the concentration distribution of the reactive species within the diffusion layer, because in the E-FeCo@NC/CF-PMS system, in addition to the optimization of the activation efficiency of the PMS, the design of the optimal solid-liquid interface is also an extremely important task to enhance the degradation efficiency of the target pollutants of the system, which determines the surface properties and reaction environment of the electrode and catalyst, such as migration, diffusion and reaction phenomena [58]. Mass transport has the potential to be a critical factor in pollutant degradation efficacy due to the continuous consumption of the target pollutant, the generation of other products, and the changes in the local environment during the reaction. Therefore, more favorable reaction interfaces need to be designed to achieve significant performance gains. However, what constitutes the local reaction environment in a system such as electrocatalytic degradation of organics in this article remains an open question. Further understanding is needed to define the physical phenomena leading to the local environment of the catalyst and adequately capture the parameters most important for performance. The mechanism in the E-FeCo@NC/CF-PMS process was proposed in Scheme 1.

3.6. Contribution of different reaction pathways in E-FeCo@NC/CF-PMS system

NB, BA and FFA were used as probe compounds to analyze the contribution of [•]OH, SO₄^{•-} and ¹O₂ quantitatively based on previous studies [30,31]. The degradation kinetics of three probe compounds was shown in Fig. S16, then the [[•]OH]_{ss}, [SO₄^{•-}]_{ss}, and [¹O₂]_{ss} were calculated through Eqs. 5–7. The results showed approximately 3.5×10^{-12} M of [[•]OH]_{ss} and 2.39×10^{-12} M of [SO₄^{•-}]_{ss} were generated during the E-FeCo@NC/CF-PMS process, whereas the yield of [¹O₂]_{ss} was 5.16×10^{-10} M, which was even two orders of magnitude higher than the steady-state concentration of [[•]OH]_{ss} and [SO₄^{•-}]_{ss}. The contribution of active species to the degradation of CBZ was further calculated through Eqs. 8–11. The *R*_{OH} and *R*_{SO₄^{•-}} were 36.15% and 5.39%, indicating that SO₄^{•-} was not the dominant radical in the degradation of CBZ. This result was consistent with the weak quenching of SO₄^{•-} in the capture experiment and the almost negligible SO₄^{•-} signal in the EPR spectrum. It is worth noting that even if there is a high concentration of ¹O₂ in the system, the calculated contribution of ¹O₂ is only 0.16%, this finding is similar to previous study [75]. This is because the second-order rate constant of CBZ and ¹O₂ is only 2.57×10^5 M⁻¹ s⁻¹, even four orders of magnitude lower than *k*_{CBZ,•OH} (8.8×10^9 M⁻¹ s⁻¹) and *k*_{CBZ,SO₄^{•-}} (1.92×10^9 M⁻¹ s⁻¹) [76]. Therefore, other effects calculated through Eq.10 (mainly including ETP, anodic oxidation, and adsorbed surface [•]OH) contributed 58.30% to the degradation of CBZ.

4. Practical application evaluation

From a practical perspective, the reusability of FeCo@NC/CF and the energy consumption of the E-FeCo@NC/CF-PMS process are critical to the remediation of contaminated water [77]. Considering this, the stability of FeCo@NC/CF was evaluated using continuous running experiments. As shown in Fig. 10 a, the removal efficiency of CBZ remains above 90% after 10 repetitions with a low amount of leaching metal (Fig. S17), indicating that E-FeCo@NC/CF can be used as an effective activation system for PMS activation. The decrease of apparent rate constant in the cycles experiments may be due to the adsorption of



Scheme 1. The proposed mechanism for CBZ degradation in the E-FeCo@NC/CF-PMS system.

catalytic intermediates on the FeCo@NC/CF surface and the loss of a few active sites. The EEC of E-FeCo@NC/CF-PMS process ($0.0506 \text{ kWh} \cdot \log^{-1} \cdot \text{m}^{-3}$) was much lower than that of E-CF-PMS process ($0.3493 \text{ kWh} \cdot \log^{-1} \cdot \text{m}^{-3}$) as shown in Table S8 and Fig. 10 c, proving that the FeCo@NC played a key role in reducing energy consumption in the removal of organic pollutant by electro-activation of PMS. In addition, the EEC of E-FeCo@NC/CF-PMS is superior to the results of similar works reported in other literature, such as $1.89 \text{ kWh} \cdot \log^{-1} \cdot \text{m}^{-3}$ of E-ACF-PMS process [28] and $0.326 \text{ kWh} \cdot \log^{-1} \cdot \text{m}^{-3}$ of E-CuFe₂O₄/GF-PS process [78]. This further demonstrates the advantages of E-FeCo@NC/CF-PMS system in reducing energy consumption and treatment cost.

In order to reflect the influence of external voltage on FeCo@NC catalyst, TEM, XRD and XPS analysis of FeCo@NC were carried out after the reaction with or without current. As shown in Fig. S18, the morphology of the catalyst after the reaction shows a good consistency in the case of adding current or not, and is similar to the freshly prepared FeCo@NC. The metal particles are uniformly dispersed in the graphite-carbon skeleton. In addition, the XRD pattern also shows the standard CoFe diffraction peak similar to that of the fresh FeCo@NC catalyst (Fig. 10d). Only the peak intensity changed slightly, and there is no diffraction peak of iron oxide or cobalt oxide, which reflects the excellent stability of FeCo@NC catalyst. The XPS characterization was carried out to further explore the surface chemical states of catalysts. As shown in Fig. 10 e-f, the ratio of $\text{Fe}^{2+}/\text{Fe}^{3+}$ and $\text{Co}^{2+}/\text{Co}^{3+}$ is 2.46 and 1.86 after the reaction at the current density of 1.6 mA cm^{-2} , which is significantly greater than the value without applying a current ($\text{Fe}^{2+}/\text{Fe}^{3+}=1.32$, $\text{Co}^{2+}/\text{Co}^{3+}=1.24$). This proves that the external electric field is beneficial to promote the regeneration of low valence metal ions, which is beneficial to promote the continued activation of PMS.

To investigate the applicability of E-FeCo@NC/CF-PMS system for different micropollutants, atrazine (ATZ, a pesticide), 2, 4-dichlorophenol (2,4-D-CP, a pharmaceutical and pesticide precursor), sulfamate dimethazine and tetracycline (SMT and TC, antibiotic contaminants) were selected as the representatives. As shown in Fig. 10 g and Fig. S19 that the E-FeCo@NC/CF-PMS process exhibited faster removal for TC, SMT and CBZ, while the removal rates of 2, 4-DCP and ATZ were lower, but still reached 90%. This is due to the ETP process more likely oxidized the pollutants with low-redox potential (TC, SMT and CBZ). The pollutants (e.g., 2, 4-DCP and ATZ) with a high redox potential were degraded primarily by radicals [31]. In general, the effective elimination

of other organic pollutants showed the prevalence of the E-FeCo@NC/CF-PMS system for effective removal of a variety of refractory pollutants. More importantly, to further evaluate the application potential of E-FeCo@NC/CF-PMS process in complex water environment, the effects of common environmentally relevant substances including inorganic anions such as SO_4^{2-} , NO_3^- , HPO_4^{2-} , HCO_3^- and humic acid (HA) on the degradation of CBZ were investigated. As shown in Fig. 8h, the removal efficiency was significantly increased after the addition of HPO_4^{2-} , which is possibly because the nucleophilic attack of phosphate on PMS led to the activation of PMS [79,80]. However, due to the inhibition of $\cdot\text{OH}$ by HCO_3^- and humic acids, the removal rate of CBZ was somewhat reduced, but still maintained at 82% and 90%, which is due to the strong resistance to inorganic ions and natural organic matter for ETP [5], suggesting that E-FeCo@NC/CF-PMS process may serve as a potential method for environmental recovery. In order to explore the applicability of E-FeCo@NC/CF-PMS system in different water substrates, five different water substrates (Deionized water, Secondary wastewater effluent, Aquaculture water, Medical waste, and lake water) were used to study the removal effect of CBZ without adjusting the pH (water quality parameters are shown in Table S9). It was found that the removal efficiency could be maintained above 90% (Fig. 10i) in all the real matrices. It is thus clear that the E-FeCo@NC/CF-PMS system has great application prospects in other actual matrices as well. It is thus clear that the E-FeCo@NC/CF-PMS process has good reusability and practical application potential in wastewater treatment.

5. Conclusions

In summary, FeCo@NC was successfully prepared by a convenient one-pot calcination method, which is simple, low cost and suitable for large-scale production. Benefit from the protection of internal metals by graphite shell and the co-existence of active components such as C-C, O-C=O and M=O groups, FeCo@NC displayed outstanding structural and catalytic stability. The co-activation of PMS by electrochemistry and FeCo@NC exhibited an outstanding synergy, which can be attributed to the activation of PMS by transition metals and the cathode itself, enhanced mass transfer, and regeneration of low-valent metal species by the cathode. It was verified by EPR analysis, capture experiment, probe experiment and electrochemical analysis that both radical and non-radical PMS activation pathways coexisted in E-FeCo@NC/CF-PMS process. In addition, the E-FeCo@NC/CF-PMS process has a low energy

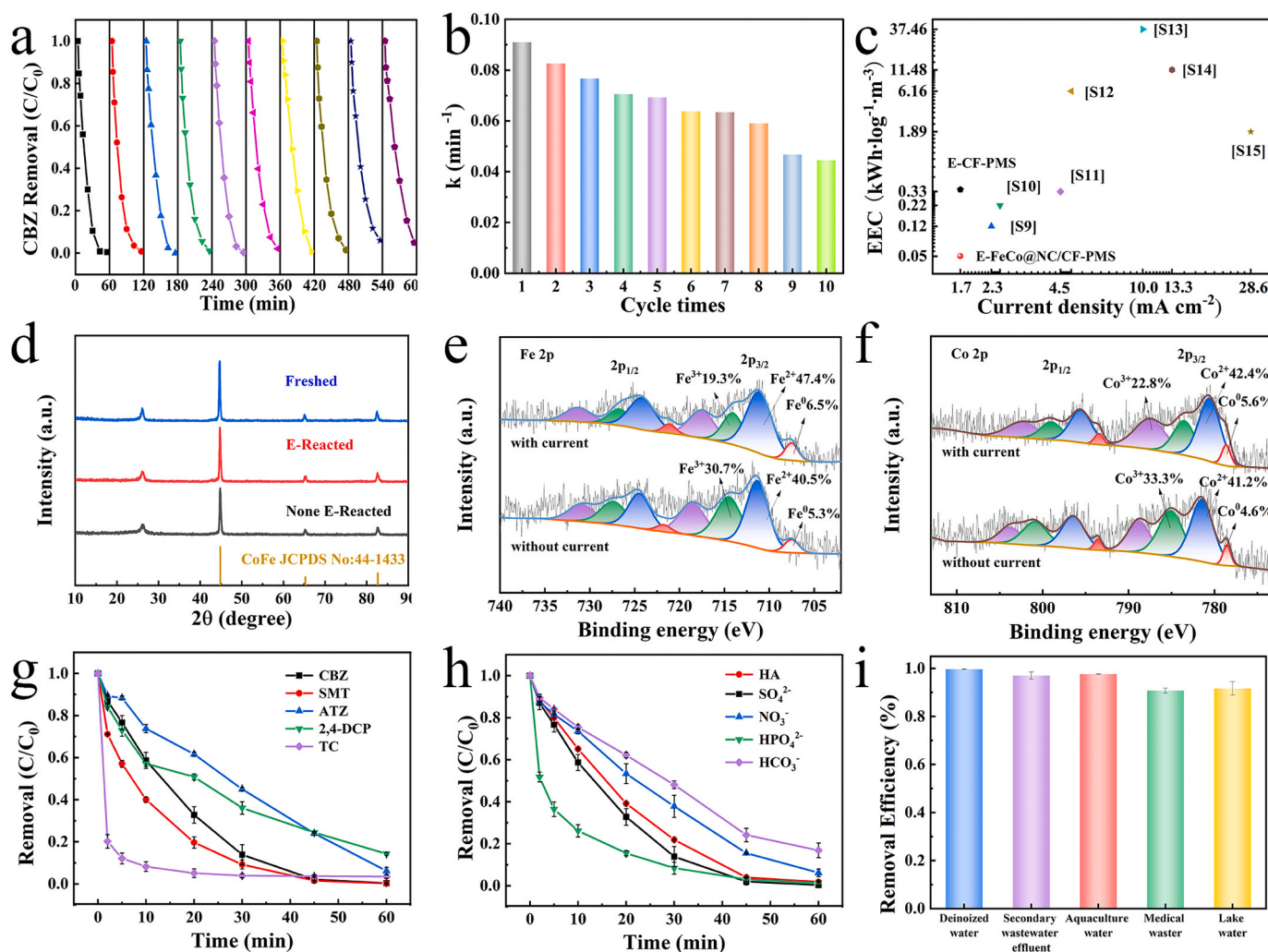


Fig. 10. (a-b) Reusability of the FeCo@NC/CF for the degradation of CBZ, (c) Comparison of EEC with other literature, (d) XRD patterns of FeCo@NC after the reaction with or without current; (e-f) High-resolution XPS spectrum of Fe 2p and Co 2p of FeCo@NC after the reaction with or without current, (g) Removal of different pollutants, (h) Influence of inorganic anions and NOM on CBZ degradation performance by FeCo@NC/CF, and (i) CBZ degradation performance by E-FeCo@NC/CF-PMS in the simulated wastewater, secondary wastewater effluent, medical wastewater and lake water of Mati lake. Reaction condition: initial concentration of different pollutants was 10 ppm, $[\text{PMS}]_0 = 1.5 \text{ mM}$, $[\text{Na}_2\text{SO}_4]_0 = 50 \text{ mM}$, $\text{pH}_0 = 7.0$, current density = 1.67 mA cm^{-2} , initial concentration of inorganic anions and NOM was 5 mM.

consumption ($0.0506 \text{ kWh} \cdot \text{log}^{-1} \cdot \text{m}^{-3}$) during organic wastewater treatment, and good adaptability to the degradation of various pollutants and remediation of actual water bodies, reflecting its potential in organic wastewater treatment. Furthermore, the system will facilitate the recovery of nano-catalysts and reduce the cost of post-treatment to promote the practical application of various high efficiency catalysts in environmental remediation.

CRediT authorship contribution statement

Shuaishuai Li: Conceptualization, Methodology, Formal analysis, Investigation, Data curation, Writing – original draft, Writing – review & editing. **Minghua Zhou:** Conceptualization, Supervision, Funding acquisition, Resources, Writing – review & editing. **Wei Wang:** Conceptualization, Supervision, Funding acquisition, Resources, Writing – review & editing. **Huizhong Wu, Ge Song and Jiana Jing:** Writing – review & editing, Data curation. **Nuo Meng:** Validation, Visualization.

Declaration of Competing Interest

It is approved by all authors and host authorities. The authors declare that there is no conflict of interest regarding the publication of this article.

Data Availability

Data will be made available on request.

Acknowledgement

This work was financially supported by Key Project of Natural Science Foundation of Tianjin (No. 21JCZDJC00320), Tianjin Key Research and Development Plan (No. 22YFYSZH00300), National Natural Science Foundation of China (Nos. 52170085 and 21976096), National High-Level Foreign Experts Project (QN20200002003, G2021125001 and G2021125002), Fundamental Research Funds for the Central Universities, Nankai University and NCC Fund.

Appendix A. Supporting information

Supplementary data associated with this article can be found in the online version at [doi:10.1016/j.apcatb.2023.123064](https://doi.org/10.1016/j.apcatb.2023.123064).

References

- [1] B.C. Hodges, E.L. Cates, J.H. Kim, Challenges and prospects of advanced oxidation water treatment processes using catalytic nanomaterials, *Nat. Nanotechnol.* 13 (2018) 642–650.
- [2] X. Duan, H. Sun, S. Wang, Metal-free carbocatalysis in advanced oxidation reactions, *Acc. Chem. Res.* 51 (2018) 678–687.
- [3] J. Wang, B. Li, Y. Li, X.B. Fan, F.B. Zhang, G.L. Zhang, W.C. Peng, Facile synthesis of atomic Fe-N-C materials and dual roles investigation of Fe-N-4 sites in fenton-like reactions, *Adv. Sci.* 8 (2021) 2101824.
- [4] H. Wang, B. Liu, Q. Si, S. Wacławek, Y. Wu, W. Jia, T. Xie, W. Guo, N. Ren, Developing functional carbon nitride materials for efficient peroxymonosulfate activation: From interface catalysis to irradiation synergy, *Environ. Funct. Mater.* 1 (2022) 21–33.
- [5] C. Liang, D. Wang, Z. Zhao, T. Li, Y. Gao, C. Hu, Coordination number dependent catalytic activity of single-atom cobalt catalysts for fenton-like reaction, *Adv. Funct. Mater.* 32 (2022) 2203001.
- [6] Y. Gao, T.W. Wu, C.D. Yang, C. Ma, Z.Y. Zhao, Z.H. Wu, S.J. Cao, W. Geng, Y. Wang, Y.Y. Yao, Y.N. Zhang, C. Cheng, Activity trends and mechanisms in peroxymonosulfate-assisted catalytic production of singlet oxygen over atomic Metal-N-C catalysts, *Angew. Chem. Int. Ed.* 60 (2021) 22513–22521.
- [7] C. Zhao, L. Meng, H. Chu, J.-F. Wang, T. Wang, Y. Ma, C.-C. Wang, Ultrafast degradation of emerging organic pollutants via activation of peroxymonosulfate over Fe₃C/Fe@N-C-x: Singlet oxygen evolution and electron-transfer mechanisms, *Appl. Catal. B Environ.* 321 (2023), 122034.
- [8] X.Y. Yu, L.J. Wang, X. Wang, H.Z. Liu, Z.Y. Wang, Y.X. Huang, G.Q. Shan, W. C. Wang, L.Y. Zhu, Enhanced nonradical catalytic oxidation by encapsulating cobalt into nitrogen doped graphene: highlight on interfacial interactions, *J. Mater. Chem. A* 9 (2021) 7198–7207.
- [9] Y.C. Wang, Y.J. Lai, L. Song, Z.Y. Zhou, J.G. Liu, Q. Wang, X.D. Yang, C. Chen, W. Shi, Y.P. Zheng, M. Rauf, S.G. Sun, S-doping of an Fe/N/C ORR catalyst for polymer electrolyte membrane fuel cells with high power density, *Angew. Chem. Int. Ed.* 54 (2015) 9907–9910.
- [10] M.A. Ahsan, A.R.P. Santiago, Y. Hong, N. Zhang, M. Cano, E. Rodriguez-Castellon, L. Echegoyen, S.T. Sreenivasan, J.C. Noveron, Tuning of trifunctional NiCu bimetallic nanoparticles confined in a porous carbon network with surface composition and local structural distortions for the electrocatalytic oxygen reduction, oxygen and hydrogen evolution reactions, *J. Am. Chem. Soc.* 142 (2020) 14688–14701.
- [11] Z. Zhao, W. Zhou, D. Lin, L. Zhu, B. Xing, Z. Liu, Construction of dual active sites on diatomic metal (FeCo–N/C-x) catalysts for enhanced Fenton-like catalysis, *Appl. Catal. B Environ.* 309 (2022), 121256.
- [12] J. Lee, U. von Gunten, J.-H. Kim, Persulfate-based advanced oxidation: Critical assessment of opportunities and roadblocks, *Environ. Sci. Technol.* 54 (2020) 3064–3081.
- [13] N. Song, S. Ren, Y. Zhang, C. Wang, X. Lu, Confinement of prussian blue analogs boxes inside conducting polymer nanotubes enables significantly enhanced catalytic performance for water treatment, *Adv. Funct. Mater.* 32 (2022) 2204751.
- [14] W.-D. Oh, Z. Dong, T.-T. Lim, Generation of sulfate radical through heterogeneous catalysis for organic contaminants removal: Current development, challenges and prospects, *Appl. Catal. B Environ.* 194 (2016) 169–201.
- [15] M.J. Huang, Y.S. Li, C.Q. Zhang, C. Cui, Q.Q. Huang, M.K. Li, Z.M. Qiang, T. Zhou, X.H. Wu, H.Q. Yu, Facilely tuning the intrinsic catalytic sites of the spinel oxide for peroxymonosulfate activation: From fundamental investigation to pilot-scale demonstration, *Proc. Natl. Acad. Sci. USA* 119 (2022), e2202682119.
- [16] S.O. Ganiyu, C.A. Martínez-Huitle, M.A. Oturan, Electrochemical advanced oxidation processes for wastewater treatment: advances in formation and detection of reactive species and mechanisms, *Curr. Opin. Electro* 27 (2021), 100678.
- [17] X. Long, Z. Xiong, R. Huang, Y. Yu, P. Zhou, H. Zhang, G. Yao, B. Lai, Sustainable Fe(III)/Fe(II) cycles triggered by co-catalyst of weak electrical current in Fe(III)/peroxymonosulfate system: Collaboration of radical and non-radical mechanisms, *Appl. Catal. B-Environ.* 317 (2022), 121716.
- [18] L.M. Jin, S.J. You, N.Q. Ren, B. Ding, Y.B. Liu, Mo vacancy-mediated activation of peroxymonosulfate for ultrafast micropollutant removal using an electrified mxene filter functionalized with Fe single atoms, *Environ. Sci. Technol.* 56 (2022) 11750–11759.
- [19] C. Yu, Z. Zhao, Y. Zong, L. Xu, B. Zhang, D. Wu, Electric field-enhanced coupled with metal-free peroxymonosulfate activator: The selective oxidation of nonradical species-dominated system, *Water Res.* 227 (2022), 119323.
- [20] F. Liu, Z. Wang, S. You, Y. Liu, Electrogenated quinone intermediates mediated peroxymonosulfate activation toward effective water decontamination and electrode antifouling, *Appl. Catal. B-Environ.* 320 (2023), 121980.
- [21] T.X. Huang, L. M. Bechelany, M. Cretin, Carbon felt based-electrodes for energy and environmental applications: a review, *Carbon* 122 (2017) 564–591.
- [22] J. Jing, X. Wang, M. Zhou, Electro-enhanced activation of peroxymonosulfate by a novel perovskite-Ti₄O₇ composite anode with ultra-high efficiency and low energy consumption: the generation and dominant role of singlet oxygen, *Water Res.* 232 (2023), 119682.
- [23] S. Sundararaman, J. Aravind Kumar, P. Deivasigamani, Y. Devarajan, Emerging pharma residue contaminants: Occurrence, monitoring, risk and fate assessment – a challenge to water resource management, *Sci. Total. Environ.* 825 (2022), 153897.
- [24] P. Su, X. Du, Y. Zheng, W. Fu, Q. Zhang, M. Zhou, Interface-confined multi-layered reaction centers between Ce-MOFs and Fe₃O₄@C for heterogeneous electro-Fenton at wide pH 3–9: Mediation of Ce³⁺/Ce⁴⁺ and oxygen vacancy, *Chem. Eng. J.* (2021), 133597.
- [25] H. Wu, Z. Hu, R. Liang, O.V. Nkwachukwu, O.A. Arotiba, M. Zhou, Novel Bi₂Sn₂O₇ quantum dots/TiO₂ nanotube arrays S-scheme heterojunction for enhanced photoelectrocatalytic degradation of sulfamethazine, *Appl. Catal. B Environ.* 321 (2023), 122053.
- [26] W. Ren, Q.M. Zhang, C. Cheng, F. Miao, H. Zhang, X.B. Luo, S.B. Wang, X.G. Duan, Electro-induced carbon nanotube discrete electrodes for sustainable persulfate activation, *Environ. Sci. Technol.* 56 (2022) 14019–14029.
- [27] I. Grčić, S. Papić, N. Koprivanac, I. Kovačić, Kinetic modeling and synergy quantification in sono and photooxidative treatment of simulated dyehouse effluent, *Water Res.* 46 (2012) 5683–5695.
- [28] Z. Liu, H.J. Ding, C. Zhao, T. Wang, P. Wang, D.D. Dionysiou, Electrochemical activation of peroxymonosulfate with ACF cathode: kinetics, influencing factors, mechanism, and application potential, *Water Res.* 159 (2019) 111–121.
- [29] L. Zhu, M. Li, H. Qi, Z. Sun, Using Fe–Cu/HGF composite cathodes for the degradation of Diuron by electro-activated peroxydisulfate, *Chemosphere* 291 (2022), 132897.
- [30] Y. Zhang, X. Chen, C. Liang, L. Yin, Y. Yang, Reconstructing the coordination environment of single atomic Fe-catalysts for boosting the Fenton-like degradation activities, *Appl. Catal. B Environ.* 315 (2022), 121536.
- [31] M. Yang, Z. Hou, X. Zhang, B. Gao, Y. Li, Y. Shang, Q. Yue, X. Duan, X. Xu, Unveiling the origins of selective oxidation in single-atom catalysis via Co–N₄–C intensified radical and nonradical pathways, *Environ. Sci. Technol.* 56 (2022) 11635–11645.
- [32] W. Ren, C. Cheng, P. Shao, X. Luo, H. Zhang, S. Wang, X. Duan, Origins of electron-transfer regime in persulfate-based nonradical oxidation processes, *Environ. Sci. Technol.* 56 (2022) 78–97.
- [33] B. Li, Q. Fang, Y. Si, T. Huang, W.-Q. Huang, W. Hu, A. Pan, X. Fan, G.-F. Huang, Ultra-thin tubular graphitic carbon nitride-carbon dot lateral heterostructures: one-step synthesis and highly efficient catalytic hydrogen generation, *Chem. Eng. J.* 397 (2020), 125470.
- [34] P. Su, W. Fu, Z. Hu, J. Jing, M. Zhou, Insights into transition metal encapsulated N-doped CNTs cathode for self-sufficient electrocatalytic degradation, *Appl. Catal. B Environ.* 313 (2022), 121457.
- [35] J.J. Hu, S. Wang, J.Q. Yu, W.K. Nie, J. Sun, S.B. Wang, Duet Fe₃C and FeN_x sites for H₂O₂ generation and activation toward enhanced electro-fenton performance in wastewater treatment, *Environ. Sci. Technol.* 55 (2021) 1260–1269.
- [36] G.H. Zhu, H.Y. Yang, Y. Jiang, Z.Q. Sun, X.P. Li, J.P. Yang, H.F. Wang, R.J. Zou, W. Jiang, P.P. Qiu, W. Luo, Modulating the electronic structure of FeCo nanoparticles in N-doped mesoporous carbon for efficient oxygen reduction reaction, *Adv. Sci.* 9 (2022) 2200394.
- [37] N. Li, R. Li, X.G. Duan, B.B. Yan, W. Liu, Z.J. Cheng, G.Y. Chen, L. Hou, S.B. Wang, Correlation of active sites to generated reactive species and degradation routes of organics in peroxymonosulfate activation by co-loaded carbon, *Environ. Sci. Technol.* 55 (2021) 16163–16174.
- [38] X.P. Sun, Z.B. Liu, Z.R. Sun, Electro-enhanced degradation of atrazine via Co-Fe oxide modified graphite felt composite cathode for persulfate activation, *Chem. Eng. J.* 433 (2022), 133789.
- [39] X. Li, F. Liao, L. Ye, L. Yeh, Controlled pyrolysis of MIL-88A to prepare iron/carbon composites for synergistic persulfate oxidation of phenol: catalytic performance and mechanism, *J. Hazard. Mater.* 398 (2020), 122938.
- [40] J. Duan, S. Chen, M. Jaroniec, S.Z. Qiao, Heteroatom-doped graphene-based materials for energy-relevant electrocatalytic processes, *ACS Catal.* 5 (2015) 5207–5234.
- [41] Q. Shi, Q. Liu, Y. Ma, Z. Fang, Z. Liang, G. Shao, B. Tang, W.Y. Yang, L. Qin, X. S. Fang, High-performance trifunctional electrocatalysts based on FeCo/Co₂P hybrid nanoparticles for zinc-air battery and self-powered overall water splitting, *Adv. Energy Mater.* 10 (2020) 1903854.
- [42] S. Cheng, H. Zheng, C. Shen, B.C. Jiang, F.Q. Liu, A.M. Li, Hierarchical iron phosphides composite confined in ultrathin carbon layer as effective heterogeneous electro-fenton catalyst with prominent stability and catalytic activity, *Adv. Funct. Mater.* 31 (2021).
- [43] P. Su, W. Fu, X. Du, G. Song, Y. Tang, M. Zhou, Nanoscale confinement in carbon nanotubes encapsulated zero-valent iron for phenolics degradation by heterogeneous Fenton: Spatial effect and structure–activity relationship, *Sep. Purif. Technol.* 276 (2021), 119232.
- [44] P. Su, M.J. Zhou, G.B. Ren, X.Y. Lu, X.D. Du, G. Song, A carbon nanotube-confined iron modified cathode with prominent stability and activity for heterogeneous electro-Fenton reactions, *J. Mater. Chem. A* 7 (2019) 24408–24419.
- [45] Q. Zhang, M. Zhou, G. Ren, Y. Li, Y. Li, X. Du, Highly efficient electrosynthesis of hydrogen peroxide on a superhydrophobic three-phase interface by natural air diffusion, *Nat. Commun.* 11 (2020) 1731.
- [46] C.Z. Wan, X.F. Duan, Y. Huang, Molecular design of single-atom catalysts for oxygen reduction reaction, *Adv. Energy Mater.* 10 (2020) 1903815.
- [47] X. Duan, Z. Ao, L. Zhou, H. Sun, G. Wang, S. Wang, Occurrence of radical and nonradical pathways from carbocatalysts for aqueous and nonaqueous catalytic oxidation, *Appl. Catal. B Environ.* 188 (2016) 98–105.

- [48] F. Chen, L.-L. Liu, J.-H. Wu, X.-H. Rui, J.-J. Chen, Y. Yu, Single-atom iron anchored tubular g-C₃N₄ catalysts for ultrafast fenton-like reaction: Roles of high-valent iron-oxo species and organic radicals, *Adv. Mater.* 34 (2022) 2202891.
- [49] S.Z. Wang, Y. Liu, J.L. Wang, Peroxymonosulfate activation by Fe-Co-O-Codoped graphite carbon nitride for degradation of sulfamethoxazole, *Environ. Sci. Technol.* 54 (2020) 10361–10369.
- [50] J. Song, N. Hou, X. Liu, M. Antonietti, P. Zhang, R. Ding, L. Song, Y. Wang, Y. Mu, Asymmetrically coordinated CoB₃N₃ moieties for selective generation of high-valence Co-Oxo species via coupled electron–proton transfer in fenton-like reactions, *Adv. Mater.* 35 (2023) 2209552.
- [51] J. Xie, C. Zhang, T.D. Waite, Hydroxyl radicals in anodic oxidation systems: generation, identification and quantification, *Water Res.* 217 (2022), 118425.
- [52] L. Bu, J. Ding, N. Zhu, M. Kong, Y. Wu, Z. Shi, S. Zhou, D.D. Dionysiou, Unraveling different mechanisms of persulfate activation by graphite felt anode and cathode to destruct contaminants of emerging concern, *Appl. Catal. B Environ.* 253 (2019) 140–148.
- [53] M.R. Powell, L. Cleary, M. Davenport, K.J. Shea, Z.S. Siwy, Electric-field-induced wetting and dewetting in single hydrophobic nanopores, *Nat. Nanotechnol.* 6 (2011) 798–802.
- [54] J.N. Israelachvili, *Intermolecular and surface forces*, Academic Pr (1992).
- [55] Y. Ge, J. Ke, X. Li, J. Wang, Q. Yang, Y. Liu, R. Guo, J. Chen, Electro-activating persulfate via biochar catalytic cathode for sulfamethazine degradation: Performance and mechanism insight, *J. Environ. Chem. Eng.* 10 (2022), 109020.
- [56] D. Bratko, C.D. Daub, K. Leung, A. Luzar, Effect of field direction on electrowetting in a nanopore, *J. Am. Chem. Soc.* 129 (2007) 2504–2510.
- [57] Q. Xu, Y. Liu, Y. Wang, Y. Song, C. Zhao, L. Han, Synergistic oxidation-filtration process of electroactive peroxydisulfate with a cathodic composite CNT-PPy/PVDF ultrafiltration membrane, *Water Res.* 210 (2022), 117971.
- [58] D. Bohra, J.H. Chaudhry, T. Burdyny, E.A. Pidko, W.A. Smith, Modeling the electrical double layer to understand the reaction environment in a CO₂ electrocatalytic system (vol 12, pg 3380, 2019), *Energy Environ. Sci.* 12 (2019), 3608–3608.
- [59] J. Leibovitz, Theorems of electrochemical mass transport in dilute solutions of mixtures of electrolytes, including weak electrolytes and hydrolysis reactions, *J. Electrochem. Soc.* 152 (2005) E282–E297.
- [60] Y. Wang, G. Yu, Challenges and pitfalls in the investigation of the catalytic ozonation mechanism: a critical review, *J. Haz. Mat.* 436 (2022), 129157.
- [61] L. Zhang, X. Jiang, Z. Zhong, L. Tian, Q. Sun, Y. Cui, X. Lu, J. Zou, S. Luo, Carbon nitride supported high-loading Fe single-atom catalyst for activation of peroxymonosulfate to generate ¹O₂ with 100% selectivity, *Angew. Chem. Int. Ed.* 60 (2021) 21751–21755.
- [62] Z. Chen, L. Wang, H. Xu, Q. Wen, Efficient heterogeneous activation of peroxymonosulfate by modified CuFe₂O₄ for degradation of tetrabromobisphenol A, *Chem. Eng. J.* 389 (2020), 124345.
- [63] X. Mi, P. Wang, S. Xu, L. Su, H. Zhong, H. Wang, Y. Li, S. Zhan, Almost 100% peroxymonosulfate conversion to singlet oxygen on Single-Atom CoN₂₊₂ sites, *Angew. Chem. Int. Ed.* 60 (2021) 4588–4593.
- [64] J. Jiang, Z. Zhao, J. Gao, T. Li, M. Li, D. Zhou, S. Dong, Nitrogen vacancy-modulated peroxymonosulfate nonradical activation for organic contaminant removal via high-valent cobalt-oxo species, *Environ. Sci. Technol.* 56 (2022) 5611–5619.
- [65] E.-T. Yun, J.H. Lee, J. Kim, H.-D. Park, J. Lee, Identifying the nonradical mechanism in the peroxymonosulfate activation process: Singlet oxygenation versus mediated electron transfer, *Environ. Sci. Technol.* 52 (2018) 7032–7042.
- [66] Y. Zong, X. Guan, J. Xu, Y. Feng, Y. Mao, L. Xu, H. Chu, D. Wu, Unraveling the overlooked involvement of high-valent cobalt-oxo species generated from the Cobalt(II)-Activated peroxymonosulfate process, *Environ. Sci. Technol.* 54 (2020) 16231–16239.
- [67] K. Chen, K. Liu, P. An, H. Li, Y. Lin, J. Hu, C. Jia, J. Fu, H. Li, H. Liu, Z. Lin, W. Li, J. Li, Y.-R. Lu, T.-S. Chan, N. Zhang, M. Liu, Iron phthalocyanine with coordination induced electronic localization to boost oxygen reduction reaction, *Nat. Commun.* 11 (2020) 4173.
- [68] C. Zhang, Y. Jiang, Y. Li, Z. Hu, L. Zhou, M. Zhou, Three-dimensional electrochemical process for wastewater treatment: A general review, *Chem. Eng. J.* 228 (2013) 455–467.
- [69] Y. Guo, Y. Ao, P. Wang, C. Wang, Mediator-free direct dual-Z-scheme Bi₂S₃/BiVO₄/MgIn₂S₄ composite photocatalysts with enhanced visible-light-driven performance towards carbamazepine degradation, *Appl. Catal. B Environ.* 254 (2019) 479–490.
- [70] J. Deng, Y.-q Cheng, Y.-a Lu, J.C. Crittenden, S.-q Zhou, N.-y Gao, J. Li, Mesoporous manganese cobaltite nanocages as effective and reusable heterogeneous peroxymonosulfate activators for carbamazepine degradation, *Chem. Eng. J.* 330 (2017) 505–517.
- [71] H. Zhou, L. Lai, Y. Wan, Y. He, G. Yao, B. Lai, Molybdenum disulfide (MoS₂): a versatile activator of both peroxymonosulfate and persulfate for the degradation of carbamazepine, *Chem. Eng. J.* 384 (2020), 123264.
- [72] Y. Hong, H. Zhou, Z. Xiong, Y. Liu, G. Yao, B. Lai, Heterogeneous activation of peroxymonosulfate by CoMgFe-LDO for degradation of carbamazepine: Efficiency, mechanism and degradation pathways, *Chem. Eng. J.* 391 (2020), 123604.
- [73] Y. Wang, L. Wu, Y. Zhou, Y. Zhang, S.-P. Sun, W. Duo Wu, X. Wang, Z. Wu, Ternary FeS/γ-Fe₂O₃@N/S-doped carbon nanohybrids dispersed in an ordered mesoporous silica for efficient peroxymonosulfate activation, *Chem. Eng. J.* 435 (2022), 135124.
- [74] S. Li, Z. Wang, X. Zhao, X. Yang, G. Liang, X. Xie, Insight into enhanced carbamazepine photodegradation over biochar-based magnetic photocatalyst Fe₃O₄/BiOBr/BC under visible LED light irradiation, *Chem. Eng. J.* 360 (2019) 600–611.
- [75] Y. Wei, J. Miao, J. Ge, J. Lang, C. Yu, L. Zhang, P.J.J. Alvarez, M. Long, Ultrahigh peroxymonosulfate utilization efficiency over CuO nanosheets via heterogeneous Cu(III) formation and preferential electron transfer during degradation of phenols, *Environ. Sci. Technol.* 56 (2022) 8984–8992.
- [76] Y. Wang, T. Pan, Y. Yu, Y. Wu, Y. Pan, X. Yang, A novel peroxymonosulfate (PMS)-enhanced iron coagulation process for simultaneous removal of trace organic pollutants in water, *Water Res.* 185 (2020), 116136.
- [77] C.A. Martínez-Huitle, M.A. Rodrigo, I. Sirés, O. Scialdone, A critical review on latest innovations and future challenges of electrochemical technology for the abatement of organics in water, *Appl. Catal. B Environ.* 328 (2023), 122430.
- [78] T. Guo, C. Dang, S. Tian, Y. Wang, D. Cao, Y. Gong, S. Zhao, R. Mao, B. Yang, X. Zhao, Persulfate enhanced photoelectrocatalytic degradation of cyanide using a CuFe₂O₄ modified graphite felt cathode, *Chem. Eng. J.* 347 (2018) 535–542.
- [79] X. Lou, L. Wu, Y. Guo, C. Chen, Z. Wang, D. Xiao, C. Fang, J. Liu, J. Zhao, S. Lu, Peroxymonosulfate activation by phosphate anion for organics degradation in water, *Chemosphere* 117 (2014) 582–585.
- [80] S. Yang, P. Wang, X. Yang, L. Shan, W. Zhang, X. Shao, R. Niu, Degradation efficiencies of azo dye Acid Orange 7 by the interaction of heat, UV and anions with common oxidants: persulfate, peroxymonosulfate and hydrogen peroxide, *J. Hazard. Mater.* 179 (2010) 552–558.